Cell Reports
Medicine

Article

Tumor-associated monocytes promote mesenchymal transformation through EGFR signaling in glioma

Graphical abstract

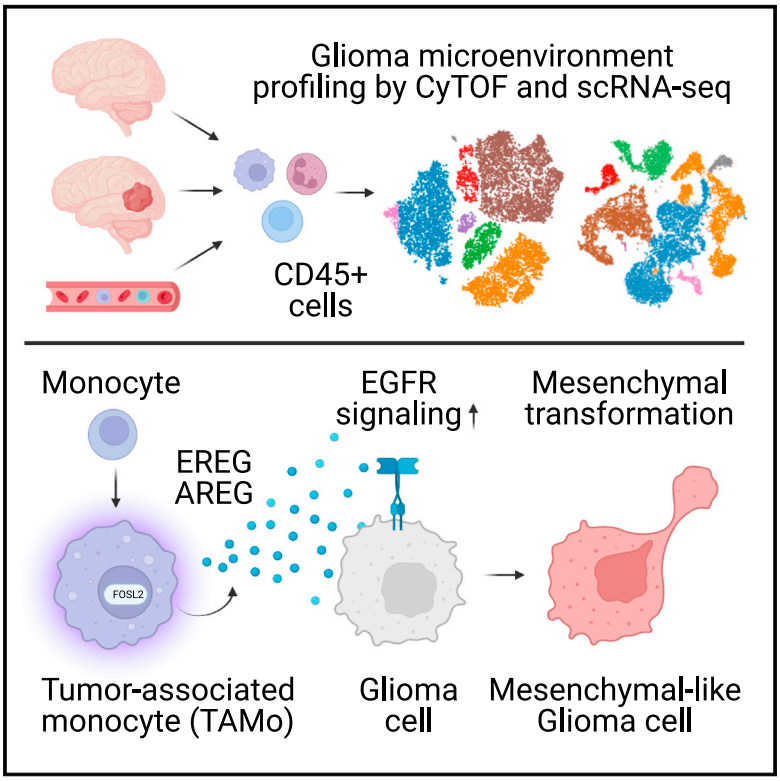

Authors

Yiyun Chen, Ran Huo, Weirong Kang, ..., Tao Jiang, Yong Cao, Jiguang Wang

Correspondence

wangwp@hku.hk (W.W.), taojiang1964@163.com (T.J.), caoyong@bjtth.org (Y.C.), jgwang@ust.hk (J.W.)

In brief

Chen et al. identify the tumor-associated monocytes (TAMo) from single-cell profiling of the immune microenvironment in glioblastoma and controls. The expression of EREG and AREG, two EGFR ligands, is activated in TAMo through regulation by FOSL2, and further activates EGFR signaling and promotes tumor cell invasion.

Highlights

- Tumor-associated monocyte (TAMo) in glioblastoma specifically expresses EREG and AREG
- TAMo is enriched in EGFR-wildtype glioblastoma and activates glioma EGFR signaling
- TAMo is associated with worse survival, necrosis, and mesenchymal transformation
- TAMo promotes glioma cell invasion through the FOSL2-EREG/AREG-EGFR axis

Chen et al., 2023, Cell Reports Medicine *4*, 101177
September 19, 2023 © 2023 The Authors.
https://doi.org/10.1016/j.xcrm.2023.101177

CellPress

Cell Reports Medicine

CellPress
OPEN ACCESS

Article

Tumor-associated monocytes promote mesenchymal transformation through EGFR signaling in glioma

Yiyun Chen,[1,2,10] Ran Huo,[3,4,10] Weirong Kang,[5,6,10] Yuwei Liu,[5,6,10] Zheng Zhao,[1,7,10] Weilun Fu,[3,4] Ruochen Ma,[1] Xiaomeng Zhang,[1] Jihong Tang,[1] Zhihan Zhu,[1] Qingyang Lyu,[5,6] Yi Huang,[5,6] Mengli Yan,[1] Biaobin Jiang,[1] Ruichao Chai,[1,2,7] Zhaoshi Bao,[3] Zheng Hu,[2,8] Weiping Wang,[5,6,*] Tao Jiang,[3,4,7,*] Yong Cao,[3,4,*] and Jiguang Wang[1,2,9,11,*]

[1]Division of Life Science, Department of Chemical and Biological Engineering, and State Key Laboratory of Molecular Neuroscience, The Hong Kong University of Science and Technology, Hong Kong SAR, China
[2]SIAT-HKUST Joint Laboratory of Cell Evolution and Digital Health, HKUST Shenzhen-Hong Kong Collaborative Innovation Research Institute, Futian, Shenzhen, China
[3]Department of Neurosurgery, Beijing Tiantan Hospital, Capital Medical University, Beijing, China
[4]China National Clinical Research Center for Neurological Diseases, Beijing, China
[5]Department of Pharmacology and Pharmacy, Li Ka Shing Faculty of Medicine, The University of Hong Kong, Hong Kong SAR, China
[6]Laboratory of Molecular Engineering and Nanomedicine, Dr. Li Dak-Sum Research Centre, The University of Hong Kong, Hong Kong SAR, China
[7]Beijing Neurosurgical Institute, Capital Medical University, Beijing, China
[8]CAS Key Laboratory of Quantitative Engineering Biology, Shenzhen Institute of Synthetic Biology, Shenzhen Institute of Advanced Technology, Chinese Academy of Sciences, Shenzhen, China
[9]Hong Kong Center for Neurodegenerative Diseases, InnoHK, Hong Kong SAR, China
[10]These authors contributed equally
[11]Lead contact
*Correspondence: wangwp@hku.hk (W.W.), taojiang1964@163.com (T.J.), caoyong@bjtth.org (Y.C.), jgwang@ust.hk (J.W.)
https://doi.org/10.1016/j.xcrm.2023.101177

SUMMARY

The role of brain immune compartments in glioma evolution remains elusive. We profile immune cells in glioma microenvironment and the matched peripheral blood from 11 patients. Glioblastoma exhibits specific infiltration of blood-originated monocytes expressing epidermal growth factor receptor (EGFR) ligands EREG and AREG, coined as tumor-associated monocytes (TAMo). TAMo infiltration is mutually exclusive with EGFR alterations ($p = 0.019$), while co-occurring with mesenchymal subtype ($p = 4.7 \times 10^{-7}$) and marking worse prognosis ($p = 0.004$ and 0.032 in two cohorts). Evolutionary analysis of initial-recurrent glioma pairs and single-cell study of a multi-centric glioblastoma reveal association between elevated TAMo and glioma mesenchymal transformation. Further analyses identify FOSL2 as a TAMo master regulator and demonstrates that FOSL2-EREG/AREG-EGFR signaling axis promotes glioma invasion *in vitro*. Collectively, we identify TAMo in tumor microenvironment and reveal its driving role in activating EGFR signaling to shape glioma evolution.

INTRODUCTION

Glioma is the most common adult brain tumor, and among different disease subtypes, isocitrate dehydrogenase (IDH)-wild-type glioblastoma (GB) is known for the worst patient prognosis and a high degree of heterogeneity. While the application of temozolomide as a first-line therapy has extended the median survival of GB to over 14 months,[1] there is still no reliable way to prevent recurrence and progression. With the rise of immunotherapy, some GB patients demonstrated promising response to immunotherapeutic strategies that boost T cell cytotoxicity, including immune checkpoint blockades,[2] neoantigen vaccines,[3] and chimeric antigen receptor T cell therapies.[4] However, achieving long-term response across large patient cohorts remains challenging, partly because of low T cell counts and the immunosuppressive microenvironment associated with GB. One key immunosuppressive factor is the presence of tumor-associated macrophages (TAMs).[5] TAM-targeted therapies such as CSF-1R inhibitor have also been developed,[6] but showed limited efficacy in clinical trials.[7] To establish efficient therapeutic strategies, a comprehensive analysis of the tumor microenvironment in GB is essential.

Single-cell immuno-profiling strategies, including mass cytometry (CyTOF) and single-cell RNA sequencing (scRNA-seq), have been extensively applied to reveal the immune compartments in different brain malignancies.[8] CyTOF profiles single cells based on dozens of immune-related protein markers. Meanwhile, scRNA-seq profiles the whole transcriptome and provides deep

This is an open access article under the CC BY-NC-ND license (http://creativecommons.org/licenses/by-nc-nd/4.0/).

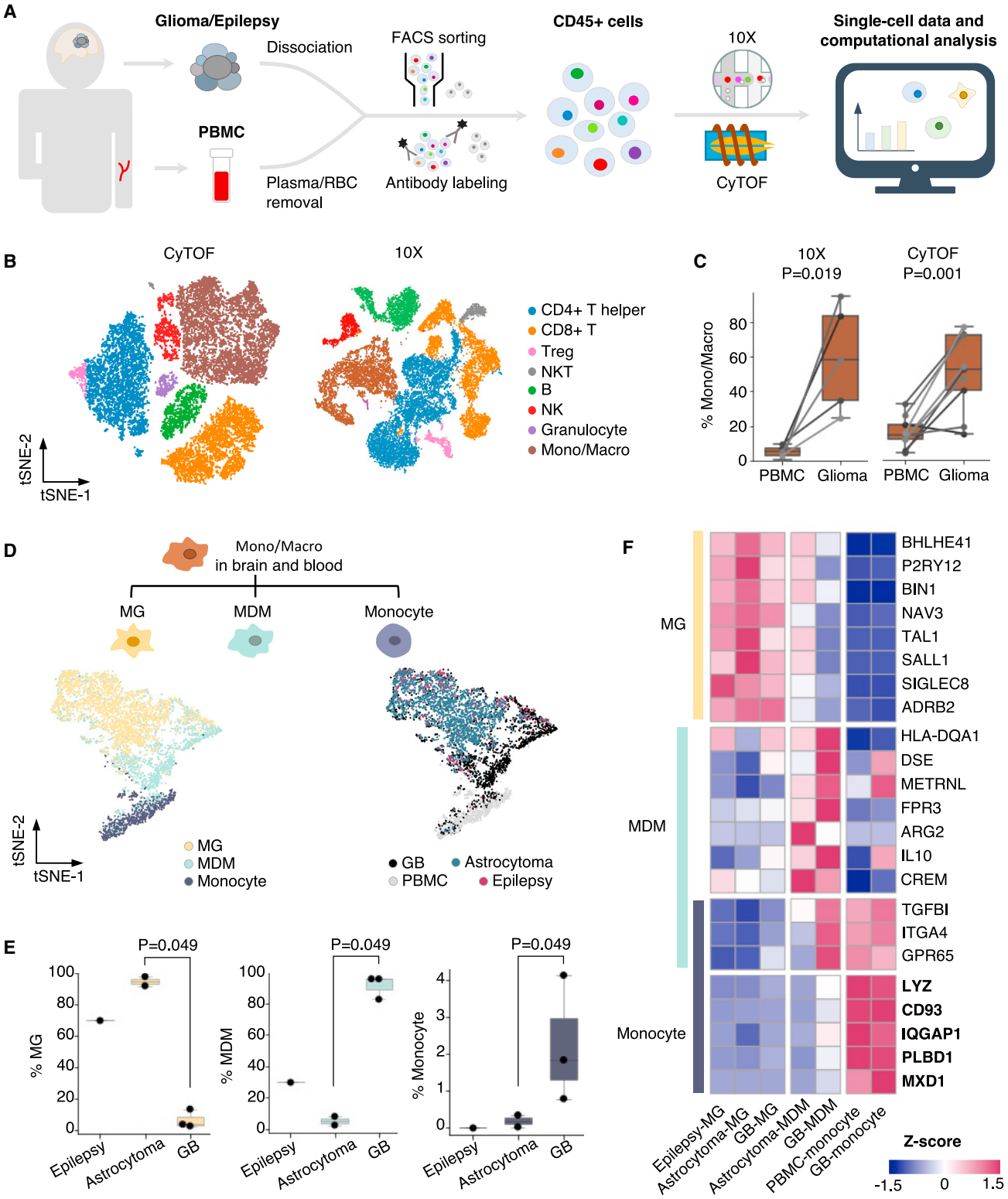

Figure 1. Resolving the immune landscape in PBMC and glioma microenvironment

(A) Workflow of the generation and analysis of immune cell landscape with 10X and CyTOF.

(B) Immune cell types identified by CyTOF and 10X.

(C) Comparison of the fraction of Mono/Macro in glioma and PBMC profiled by 10X and CyTOF. The p-values were calculated by two-tailed paired t-test.

(legend continued on next page)

CellPress
OPEN ACCESS

insights into the molecular pathways involved in the disease. Both platforms are promising tools for the analysis of the GB microenvironment, used alone or in conjunction.[9–15] Previous CyTOF and scRNA-seq studies have profiled the immune microenvironment of IDH-wildtype GB and IDH-mutant astrocytoma, highlighting their differences in the abundance of the monocyte-derived macrophages (MDMs) and the brain-resident microglia (MG).[10–12,15] However, there is limited knowledge regarding the minor immune cell types, including T cells and natural killer (NK) cells, which might be better captured in an immune-centric dataset. Moreover, without including control immune populations located outside of the tumor, the tumor-induced transcriptome reprogramming has not been fully described. Our study aimed to provide an integrated landscape of immune cells in glioma and control samples, including peripheral blood mononuclear cells (PBMCs) and tumor-free brain samples, which aided discovery of tumor-specific changes in immune cell populations as potential therapeutic targets.

Here we collected paired tumor and PBMC from 11 glioma patients and profiled the CD45$^+$ immune cells using CyTOF and/or scRNA-seq (10X Genomics) (Table S1). First, we observed enrichment of monocytes and macrophages (Mono/Macro) in the intracranial immune microenvironment compared with PBMC. The Mono/Macro populations were highly diverse in origin and function and could be classified into three subgroups: monocyte, MDM, and MG. Both monocytes and MDMs originated from blood and were more abundant in IDH-wildtype GB compared with the MG-dominated IDH-mutant astrocytoma and non-tumor brain tissue (from a patient with epilepsy). Moreover, trajectory analysis revealed that, after infiltrating into GB, certain monocytes transitioned into the EREG/AREG-expressing tumor-associated monocytes (TAMo). Over-expression of these two epidermal growth factor receptor (EGFR) ligands in TAMo was associated with the mesenchymal subtype (expression-based glioma subtyping proposed by Verhaak et al.[16]), and mutual exclusivity of *EGFR* alterations and TAMo infiltration suggested that TAMo is sufficient to activate EGFR signaling in *EGFR*-wildtype GB. In multi-centric GB and longitudinally collected glioma samples, elevation in TAMo infiltration was also correlated with mesenchymal transformation. Transcriptional network analysis pinpointed FOSL2 as a master regulator of TAMo and regulated the expression of EREG and AREG, hence providing a potential mechanism of TAMo formation. Furthermore, we demonstrated that the roles of FOSL2-EREG/AREG-EGFR axis in promoting GB cell invasion using trans-well and three-dimensional (3D) spheroid models. Altogether, our study provided a landscape of the immune cell types and states in GB and identified TAMo as a tumor-specific immune cell subtype that functions in promoting EGFR signaling and tumor invasion through secretion of EREG and AREG. This discovery lays the foundation for future development of TAMo-targeting immunotherapy.

RESULTS

Comparison of immune cell populations between glioma and matched PBMC

To enhance the capture of immune cells in 11 glioma patients and their paired PBMC (Table S1), the CD45$^+$ immune populations were enriched and profiled by scRNA-seq and/or CyTOF (Figure 1A). While CyTOF profiled 33 cell-surface protein markers (Table S2) of immune cells from nine glioma patients and provided the overall landscape of immune cell types, scRNA-seq was applied in samples from three IDH-wildtype GB, two IDH-mutant astrocytoma, and one epilepsy patients to profile the whole transcriptome and generate mechanistic insights. Using this combinational approach, our study aimed to discover recurrent patterns of immune dysfunctions in GB to provide insights for immunotherapy developments. Quality control, data preprocessing and cell type classification and quantification were first conducted on individual samples, followed by merging and batch effect correction. As a result, 17,740 cells profiled by CyTOF and 21,240 cells profiled by scRNA-seq were retained for further analyses. To ensure consistency, identification of major immune cells from two platforms were based on the same criteria, using the combinations of conventional markers[17] (Figures S1A and S1B; Table S3).

After data integration, cells co-clustered by cell type identity, regardless of their tissue of origin, although their proportions varied between glioma and PBMC (Figures 1B and S1C–S1F). Consistent with previous report that Mono/Macro are the most abundant immune cell type and constitutes 50% of cell population in high-grade glioma.[10] Mono/Macro are the most abundant and most significantly enriched immune populations in glioma compared with PBMC (Figure 1C). As for the lymphoid cells, T and NK cells also constituted a large proportion of glioma-infiltrating immune cells, while B cells poorly infiltrated into glioma (Figure S1G). Thus, our data confirmed major differences in the immune composition in the brain and peripheral blood.

Identification and characterization of lymphoid cell subtypes in GB and PBMC

The lymphoid cells, including T and NK cells, are known to play important roles in immune surveillance and elimination of tumor. In our scRNA-seq dataset, T and NK cells were rarely detected in epilepsy and astrocytoma, but were able to infiltrate into GB (Figure S1F), potentially permitted by the damage to the blood-brain barrier, which more frequently occurred in the high-grade glioma. To identify their functional states in GB, we performed unbiased clustering and assigned the subtype identity to the T and NK cells profiled by scRNA-seq, based on classical immune subtype markers[17] and prediction by SingleR[18] (Figures S1H and S1I). This approach further revealed heterogeneity in immune

(D) The subtype (left) and sample of origin (right) of Mono/Macro profiled by 10X.
(E) Boxplot comparing the fractions of MG, MDM, and monocyte in epilepsy and glioma patients profiled by 10X. The p-values were calculated by Wilcoxon rank-sum test.
(F) Heatmap illustrating the MG-, MDM-, and monocyte-specific markers expression. Each row represents one marker gene, and the left annotation bar indicates whether the marker is MG-, MDM- or monocyte-specific. Abbreviations: FACS, fluorescence-activated cell sorting.
See also Figures S1 and S2 and Tables S1–S3.

cell subtypes and states, as well as their preference in localization in PBMC versus GB. One of the GB-enriched cluster was the KLRG1$^+$CD8$^+$ central memory T cell (Tcm), which resembled the classical Tcm[19] (CD27$^+$CCR7$^+$SELL$^+$CX3CR1$^-$), but expressed higher levels of *KLRG1* and cytotoxicity markers (*PRF1*, *GZMA*, and *GZMH*) and lower levels of CD127/IL7R than the KLRG1-CD8$^+$ Tcm subgroup (Figures S1H and S1I). The KLRG1$^+$CD8$^+$ Tcm and KLRG1$^-$CD8$^+$ Tcm subsets identified in our study corresponded well with the short-lived effector cells (IL7R-KLRG1$^+$) and memory precursor effector cells (IL7R$^+$KLRG1$^-$), respectively, which differ in their half-life, response rate, and cell fate.[19,20] In contrast, the B cell and naive T cell populations were specifically found in PBMC.

Two populations of NK cells were identified, in line with two classes of cytotoxic (CD56^{dim}CD16$^+$) and immature (CD56$^+$CD16$^-$) NK cells reported previously.[21] While the cytotoxic NK cells highly expressed cytotoxicity markers (*PRF1* and *GZMB*) and were more abundant in PBMC, the immature NK cells had low cytotoxic activity and showed significant enrichment in GB (Figures S1J and S1K). The accumulation of immature NK cells in *IDH*-wildtype glioma in contrast with PBMC,[22] *IDH*-mutant glioma and brain metastases was also reported in a recent CyTOF-based study.[12] Using our scRNA-seq data, we further identified elevated expression of chemokines (*XCL1* and *XCL2*), major histocompatibility complex class II (*HLA-DRA*) and inhibitory receptors (*NKG2A/KLRC1*) in immature NK cells. The immature NK subtype was also found to be enriched in non-small cell lung cancer and demonstrated low capability of tumor killing.[23] The *NKG2A/KLRC1* was involved in inhibition of NK cytotoxicity, and anti-NKG2A therapy has demonstrated efficient NK cell activation and tumor shrinkage in preclinical and clinical settings.[24,25] While the functions of immature NK cells in GB have not been elucidated in previous studies, our analysis suggested that immature NK cells may be a population of suppressed NK cells and pinpointed potential involvement of *NKG2A* in immunosuppression.

Identification of monocyte infiltration in GB microenvironment

To better resolve the origins of Mono/Macro, we applied the ontogeny-specific marker-based approach that has been previously applied to distinguish MG and MDM.[11] As the previous study only included Mono/Macro from GB samples, we first examined the validity of this approach on all Mono/Macro cells collected from control and glioma samples. Based on ontogeny-specific marker expression,[11] three stable clusters were observed, as suggested by the highest cophenetic correlation value, as well as by visual inspection of principal component analysis (Figures S2A and S2B). The first principal component distinguished the ontogeny of Mono/Macro, which was similar to previous results,[11] with MG markers (*P2RY12* and *NAV3*) and MDM markers (*ITGA4* and *TGFBI*) enriched at opposite ends of the spectrum (Figure S2C). The decrease of the second principal component captured the monocyte-to-macrophage transition, with the preferred expression of MHC class II molecule *HLA-DQA1* in MDM and *LYZ* in monocytes, respectively. Thus, by including PBMC as control, three Mono/Macro subtypes were identified to represent the MG, MDM, and monocyte, which expanded the dichotomic classification in previous studies (Figure 1D). The enrichment of monocyte in PBMC and MG in epilepsy was consistent with previous knowledge, supporting the robustness of the method in distinguishing the three cell subtypes in our dataset. Moreover, while MG were present in both glioma and non-cancerous brain, the GB-infiltrating MG demonstrated elevated expression of genes associated metabolic (*APOC1*), inflammatory (*CD163* and *CEBPD*), interferon signaling (*TNFAIP3*), and antigen presentation (*HLA-DRB5* and *HLA-DMA*) pathways (Figure S2D). These observations are consistent with previous reports[13,26] and suggest that tumor-mediated effects can alter MG functions.

Noticeably, both monocyte and MDM fractions were significantly elevated in GB compared with epilepsy and astrocytoma, while MG proportion was significantly lower (Figure 1E). Independent single-cell datasets[15,27] and immunostaining-based methods[28] also supported the presence of a group of HLA-DR-negative monocyte-like populations in GB. We then estimated and compared the abundance of the three Mono/Macro subtypes in TCGA glioma samples based on specific markers in bulk RNA-seq (Figure 1F). Consistent with observations from our single-cell dataset and other studies,[12] increased MDM infiltration was observed in gliomas of higher grade, *IDH*-wildtype subtype and mesenchymal transcriptome subtype, while MG fraction was decreased (Figure S2E). Interestingly, monocyte infiltration was also elevated in high-grade, *IDH*-wildtype, and mesenchymal glioma, suggesting its associations and potential functions in promoting more aggressive tumor phenotypes.

TAMo with elevated EREG and AREG expression is specifically detected in GB

To study the dynamic changes and transcriptional programs involved in the MDM and monocyte reprogramming, we performed further analyses of monocytes and MDMs collected from PBMC and GB. A large fraction of infiltrated monocytes was activated and differentiated into MDM, which can be further categorized into four clusters, namely NR4A3$^+$ MDM, FN1$^+$ MDM, INKA1$^+$ MDM, and MRC1$^+$ MDM, based on unsupervised clustering, suggesting heterogeneity within the MDM subset (Figure 2A). Starting from the PBMC monocytes, the four subsets of MDM also showed differences in the paths and locations on the inferred trajectories (Figures 2B and S2F). Nevertheless, they shared common characteristics including over-expression of macrophage differentiation markers (FCGR3A, HLA-DQA1, C1QA, and IGF1), TREM2, and CSF1R (Figure 2A), suggesting they could be depleted by anti-TREM2 and anti-CSF1R therapy in GB.[15,29]

In contrast, the monocytes found in GB samples, hereafter termed TAMo, were more similar to monocytes found in the blood and demonstrated lower level of expressions of TREM2, CSF1R, and macrophage differentiation markers (Figure 2A). More important, TAMo followed a different trajectory from the MDM clusters (Figures 2B and S2E), and they demonstrated a distinct transcriptional profile from MDM and PBMC-monocyte with elevated expression of EGFR ligands (*EREG* and *AREG*), pro-angiogenesis factors (*LRG1* and *VEGFA*), chemokine *CXCL2*, and scavenger receptor *MARCO* (Figure 2A). Based on these TAMo-specific markers, we calculated the TAMo score

CellPress
OPEN ACCESS

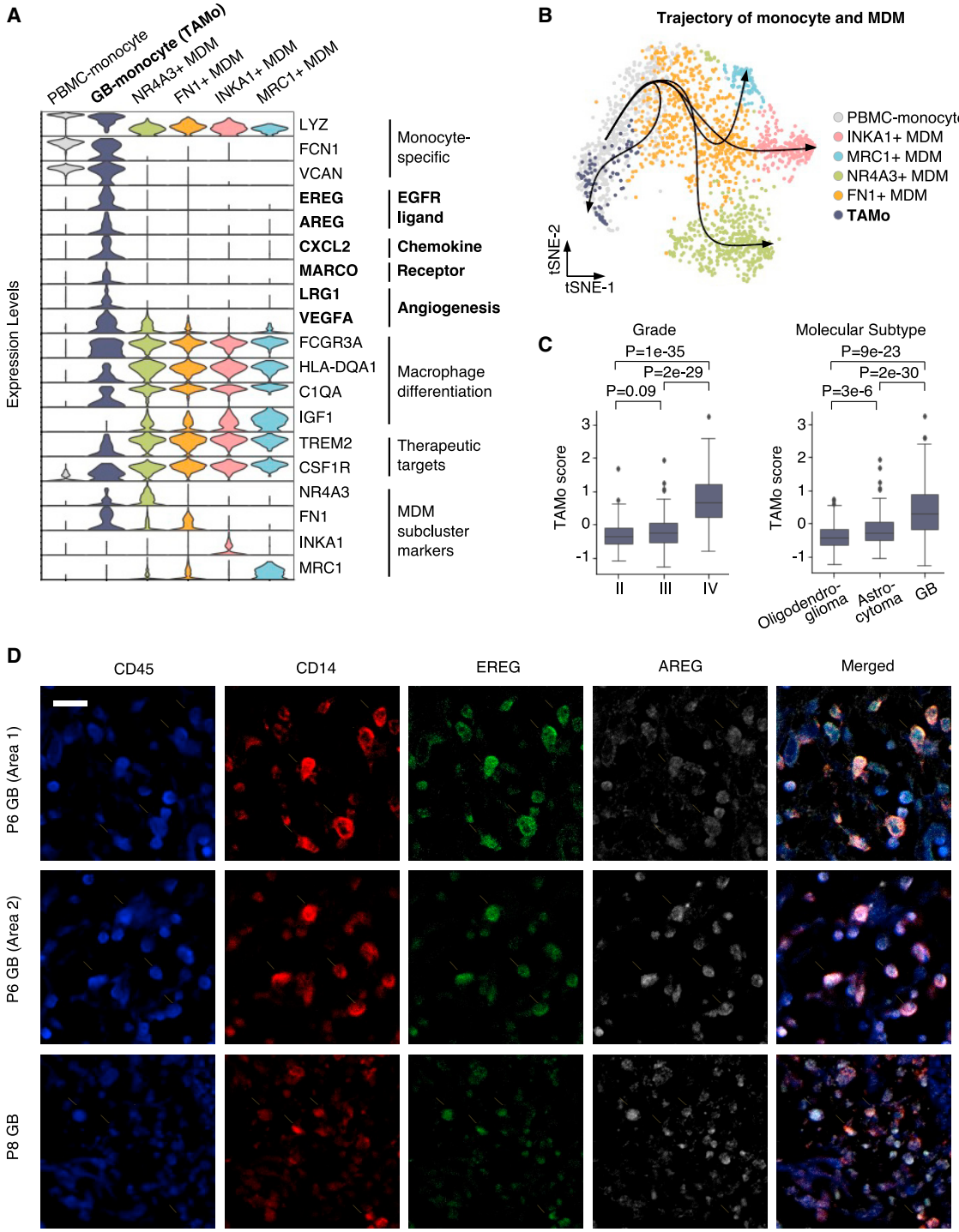

Figure 2. TAMo specifically expressed *EREG* and *AREG*

(A) Violin plots highlighting the differentially expressed genes in different clusters, as well as their potential functions. The TAMo-specific genes are highlighted in bold.

(B) Developmental trajectory of monocytes and MDM clusters. The black curves represented the trajectory predicted by Slingshot.

(C) Comparison of TAMo score in patients of different glioma grade and molecular subtype in the TCGA dataset. p values were calculated by Wilcoxon rank-sum test.

(D) Representative images of GB samples simultaneously stained with CD45, CD14, EREG, and AREG antibodies. The arrowhead highlights cells with strong signals for all four channels. Scale bar, 20 μm.

See also Figure S2.

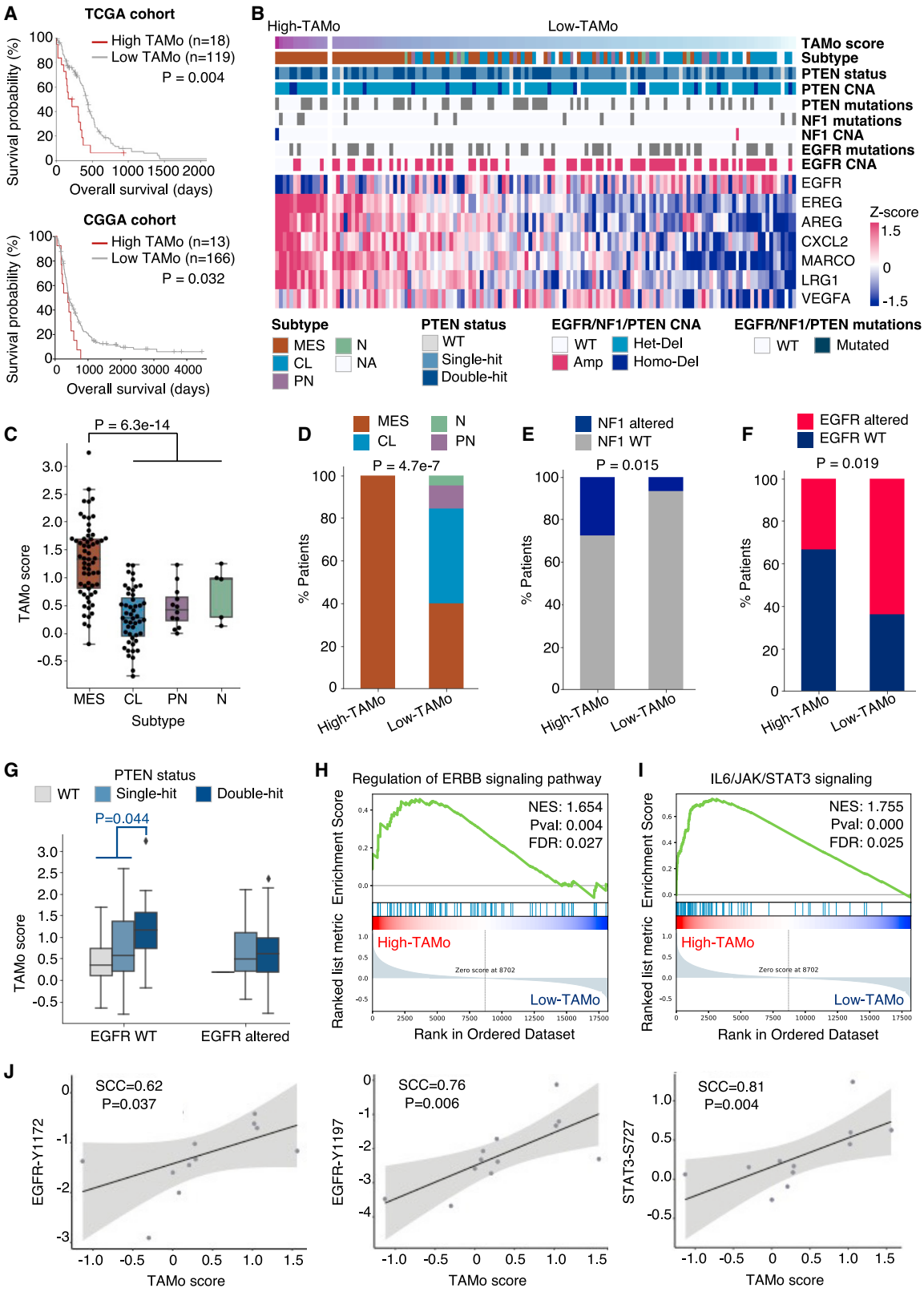

(legend on next page)

CellPress
OPEN ACCESS

in glioma patients in the TCGA cohort and observed that TAMo was significantly enriched in high-grade, IDH-wildtype GB (Figure 2C).

Of the list of TAMo signature genes, EREG and AREG were the top two most significantly upregulated genes in TAMo and both are known to be ligands of EGFR. As there has not been any *in vivo* evidence or characterization of this cell population in previous studies, multicolor staining of tumor sections from these GB patients was performed and the results validated the presence of a population of Mono/Macro ($CD45^+CD14^+$) that co-expressed EREG and AREG proteins (Figure 2D). Thus, our study defined TAMo as a subgroup of Mono/Macro specifically enriched in GB and with potential functions in promoting EGFR signaling in the tumor cells.

Cross-sectional analysis reveals involvement of TAMo in EGFR signaling and mesenchymal transformation

Previous studies have shown that neither MG nor MDM fraction were prognostic in GB patients.[11,12] We found that the TAMo score distinguished a subset of GB with significantly worse overall survival in the TCGA cohort (Figure 3A, top), which was validated in an independent cohort from the Chinese Glioma Genome Atlas[30,31] (Figure 3A, bottom). Furthermore, in the GB patients with a high TAMo score, we identified enrichment of glioma of the mesenchymal subtype and harboring *NF1* alterations (Figures 3B–3E). While the EGFR ligands were highly expressed, the *EGFR* gene was less frequently mutated or amplified in the GB patients with high TAMo infiltration, and *EGFR* also demonstrated lower expression in these patients (Figures 3F and S3A). Homozygous loss-of-function alterations in *PTEN* were also associated with higher TAMo infiltration in EGFR wild-type GB (Figure 3G), compatible with recent reports.[32,33]

It is worth mentioning that *EREG* and *AREG* expression was negatively correlated with *EGFR* expression and downregulated in *EGFR*-altered tumor (Figure S3B), and such mutual exclusivity suggest functional redundancy. Moreover, Gene Set Enrichment Analysis revealed a significantly higher EGFR (also known as ERBB) pathway activity in patients with high TAMo score (Figure 3H), suggesting that the infiltration of TAMo may be sufficient for generating a high concentration of EGFR ligands and, thus, activate the EGFR signaling in glioma in an *EGFR*-alteration-independent manner. Elevated activity of STAT3 signaling, which is one of the downstream pathways of EGFR, was also observed in the high-TAMo GB patients, thus linking EGFR activation to STAT3-mediated mesenchymal transformation in GB[34] (Figures 3H and 3I). To directly correlate TAMo scores with EGFR-STAT3 signaling activities at the protein level, we explored an independent proteomic dataset CPTAC[35] and revealed significant positive correlations between TAMo score and phosphorylated EGFR and STAT3 in IDH-wildtype EGFR-wildtype GB patients (Figure 3J). The EGFR protein and RNA levels tend to positively correlate with TAMo score in EGFR-wildtype GB (not significant), while negative correlations were observed when EGFR-altered cases were included (Figure S3C). Collectively, our analyses suggest that, while EGFR-altered tumor generally showed high level of EGFR expression and limited dependency on tumor-extrinsic factors for EGFR pathway activation, the EGFR-wild-type tumor are more responsive to activation by EGFR ligands secreted by TAMo.

To study whether the induction of TAMo signature expression in PBMC-monocyte was common across the 137 IDH-wildtype GB patients from TCGA cohort, we analyzed the correlations between TAMo signatures and the monocyte-specific markers that were expressed in both PBMC-monocyte and TAMo. While a strong positive correlation was observed, a subgroup of patients with high monocyte but low TAMo score, here defined as the High-Mono Low-TAMo group, was identified (Figure S3D). This subgroup of patients demonstrated significantly higher level of *EGFR* expression, a larger fraction of *EGFR* mutant or amplified cases, and better survival than patients in the High-TAMo group (Figures S3E–S3H). The results hinted that the TAMo signature was the key contributor to worse survival in high-TAMo subgroup of GB patients, rather than the general infiltration levels of monocytes.

Spatiotemporal dynamics of TAMo correlates with mesenchymal transformation

Intratumoral heterogeneity drives tumor recurrence and progression.[36–38] Among the transcriptome subtypes of glioma, the mesenchymal subtype displays associations with worse survival outcome,[39] and the transformation of non-mesenchymal glioma into the mesenchymal was frequently observed during glioma progression.[36,40] The roles of tumor-extrinsic factors[41,42] in mesenchymal transformation await to be further explored. In

Figure 3. TAMo was associated with elevated EGFR signaling in GB

(A) Associations between TAMo score and the overall survival in IDH-wildtype GB patients in TCGA (top) and Chinese Glioma Genome Atlas (CGGA) (bottom) cohorts. The patients were group into high TAMo (with TAMo score >1.65) and low TAMo (TAMo score <1.65) in both cohorts. p values were calculated by log-rank test.

(B) Heatmap of TAMo marker and *EGFR* gene expression in IDH-wildtype GBM samples in TCGA cohort. The patients were ranked by TAMo score, and the subtype and genetic alterations were marked on top of the heatmap.

(C) Comparison of TAMo score in patients of different transcriptome subtypes. p value was calculated by Wilcoxon rank-sum test.

(D–F) Comparisons of the fractions of patients of different transcriptome subtypes (D), *NF1* (E), and *EGFR* alteration status (F) in the high-TAMo versus low-TAMo groups. p values were calculated by two-tailed Fisher's exact test.

(G) Comparison of TAMo score in EGFR-wildtype and EGFR-altered patients with different PTEN mutation status. p value was calculated by Wilcoxon rank-sum test.

(H and I) Gene set enrichment analysis of ERBB signaling pathway (H) and JAK/STAT3 signaling (I) between GBM patients in high-TAMo versus in low-TAMo groups.

(J) Spearman's correlation coefficient (SCC) and p values between phosphorylated EGFR, phosphorylated STAT3 and TAMo score in IDH-wildtype EGFR-wildtype GB patients in the CPTAC dataset. Abbreviations: CL, classical subtype; FDR, false discovery rate; MES, mesenchymal subtype; N, neural subtype; PN, proneural subtype.

See also Figure S3.

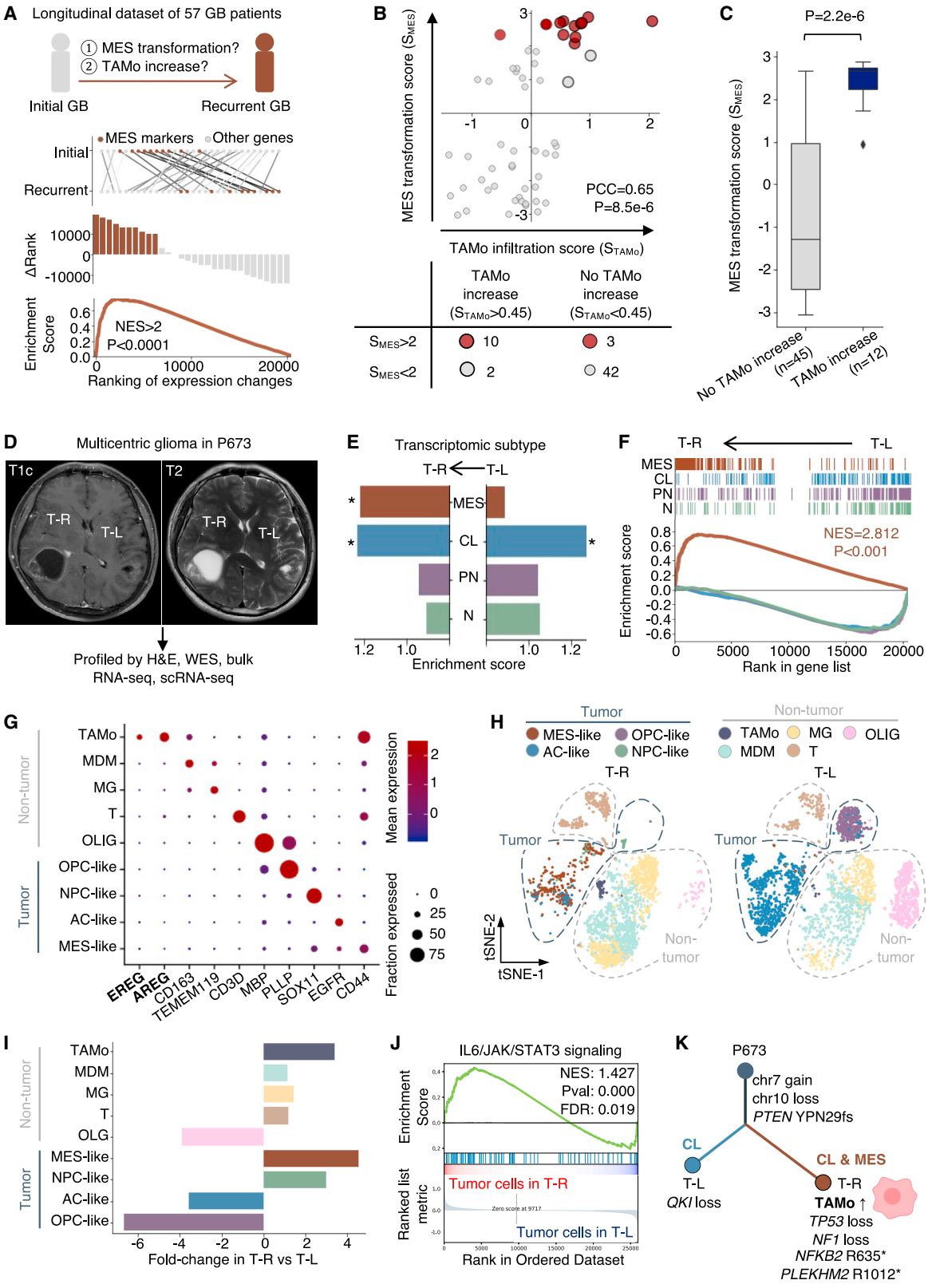

(legend on next page)

CellPress
OPEN ACCESS

our study, the enrichment of TAMo in mesenchymal GB in the cross-sectional cohort also hinted their association with the mesenchymal subtype.

To trace the dynamics of subtype switching and explore the role of TAMo infiltration in this process, we designed a rank-based approach to assess the shift toward mesenchymal subtype between two temporally or spatially separated samples (Figure 4A and STAR Methods). Re-analyzing 57 GB patients with longitudinally collected glioma pairs,[36] we identified 13 patients with mesenchymal transformation during recurrence. In 10 of the 13 patients, increase in TAMo score was observed during mesenchymal transformation (Figures 4B and S4A). Meanwhile, in patients with increased TAMo level during recurrence, a significantly higher mesenchymal transformation score was observed (Figure 4C). These results suggest the involvement of TAMo in mesenchymal transformation.

While measurements in longitudinal data could be affected by systematic changes in immune functions under radio-chemotherapy, we analyzed patient P673 with multicentric glioma at the genomics, transcriptomic and cellular levels (Figure 4D). Two tumors were identified in this patient and surgically removed around the same time, including one tumor with 59.23 mL volume on the right and another with volume of 11.23 mL on the left side (hereafter named as T-R and T-L, respectively). Both tumor samples were molecularly classified as the *IDH*-wildtype GB with *TERT* promoter mutation (C250T), chromosome $7^{+}/10^{-}$ by the World Health Organization in 2021, but T-R showed more aggressive necrosis phenotypes. Comparing mesenchymal markers in their bulk transcriptomes, T-R showed significant enrichment of both classical and mesenchymal signatures, while the T-L was classical subtype (Figure 4E). Compared with T-L, T-R showed a remarkable elevation of mesenchymal transformation score (Figures 4F and S4B).

Our recent work generated single-cell RNA-seq data of these two samples,[43] and we further characterized the tumor cellular states as well as immune microenvironment differences in T-R and T-L. The tumor and non-tumor cells were first segregated by their copy number variation profiles, and the tumor cells were further resolved into four subtypes as previously described[44] (Figures 4G, 4H, S4C and S4D). The copy number variation inferred from single-cell RNA-seq aligned well with the chromosome 7 gain and 10 loss identified from whole-exome sequencing (Figure S4D). Chromosome 7 gain was detected in most tumor cells classified as astrocyte-like (AC-like), mesenchymal-like (MES-like), and neural-progenitor-like (NPC-like), while the oligodendrocyte-progenitor-like (OPC-like) cells either did not carry chromosome 7 gain or did not over-express the genes located on this chromosome (Figure S4D). Among the non-tumor cells, we also identified a cluster of TAMo-like cells with elevated expression of *EREG* and *AREG*, while other cell types showed low expression (Figure 4G). Comparing their cell fractions, T-L was mainly composed of the AC-like and OPC-like cells, while the MES-like cells were more dominant in T-R (Figures 4H and 4I). The increase in TAMo score accompanied the mesenchymal transformation and more aggressive histological phenotypes in T-R in contrast with T-L, while other immune cells remain similar. Tumor cells in T-R also demonstrated enrichment of STAT3 signaling (Figure 4J), which is one of the downstream pathways of EGFR activation and is involved in glioma mesenchymal transformation. Integration of the genomic, transcriptome and cellular landscape of this multicentric glioma case suggested that TAMo is a potential factor involved in the formation of mesenchymal GB (Figure 4K).

FOSL2 is a master regulator of TAMo

Transcriptional factors (TFs) play important roles in programming cell type identity and states. To disentangle the tumor-induced changes in the transcriptional network of TAMo and MDM, we inferred the TF activity from the single-cell transcriptome data by SCENIC.[45] The activity of each TF and their regulated targets,

Figure 4. TAMo was associated with mesenchymal transformation

(A) Characterization of the mesenchymal (MES) transformation process in longitudinal GB patients. From top to bottom: description of longitudinal dataset with paired initial and recurrent GB samples from the same patient; rank of MES markers (maroon) and other genes (gray) in initial and recurrent GB, with ranks of the same gene in different samples connected by lines; change of rank (ΔRank) of MES markers (maroon) and other genes (gray) in recurrent versus initial sample; enrichment score (ES), normalized enrichment (NES) and p value of MES markers by single sample Gene Set Enrichment Analysis (ssGSEA) analysis of the gene expression rank-change between initial and recurrent sample.

(B) The correlation between MES transformation and TAMo infiltration during recurrence (top) and number of patients in each category (bottom). Pearson's correlation coefficient (PCC) and p value between MES transformation score (S_{MES}) and TAMo infiltration score (S_{TAMo}) are shown.

(C) Comparison of MES transformation score in patients with increased TAMo infiltration versus with no TAMo increase. p value was calculated by Wilcoxon rank-sum test.

(D) MRIs of the multicentric glioma patient P673 before surgery. The location of the right-brain tumor (T-R) and left-brain tumor (T-L) of the patient were labeled.

(E) The enrichment score of the four glioma transcriptome subtypes inferred from the bulk RNA-seq data of the T-R (left) and T-L (right) samples of patient P673. The asterisks mark the significant subtypes ($p < 0.05$) in the sample.

(F) Analysis of changes in the four transcriptome subtypes based on gene expression rank-change between T-R and T-L. The NES and p-value of mesenchymal signature was shown.

(G) Representative markers of different tumor and non-tumor clusters identified in scRNA-seq data of patient P673. The dot color and size represented the mean expression and the fraction of cells expressing the markers.

(H) The t-SNE plot of cells identified from scRNA-seq of the T-R and T-L samples of patient P673. The tumor and non-tumor clusters were outlined to ease visualization and comparison.

(I) Fold-change in the fraction of each cell type in T-R versus in T-L.

(J) Gene Set Enrichment Analysis (GSEA) analysis of JAK/STAT3 signaling pathways in tumor cells from T-R versus T-L.

(K) The evolution of T-L and T-R tumor in patient P673. The oncogenic mutations and significant transcriptome subtypes of the two tumor were indicated in the plot.

See also Figure S4.

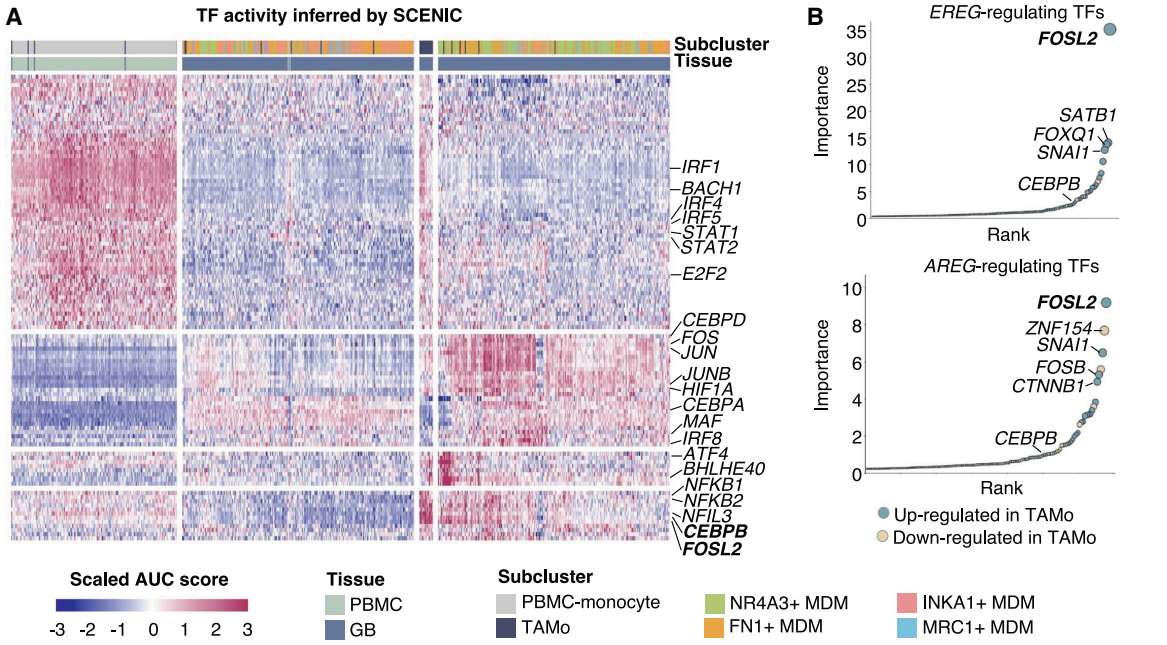

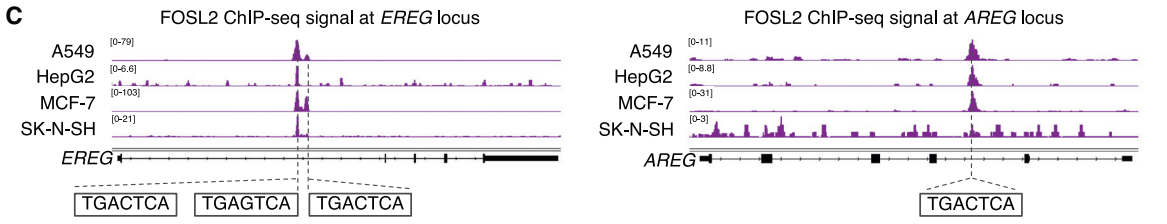

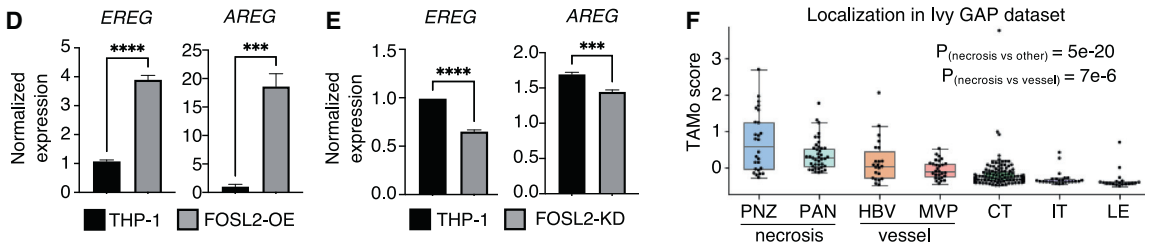

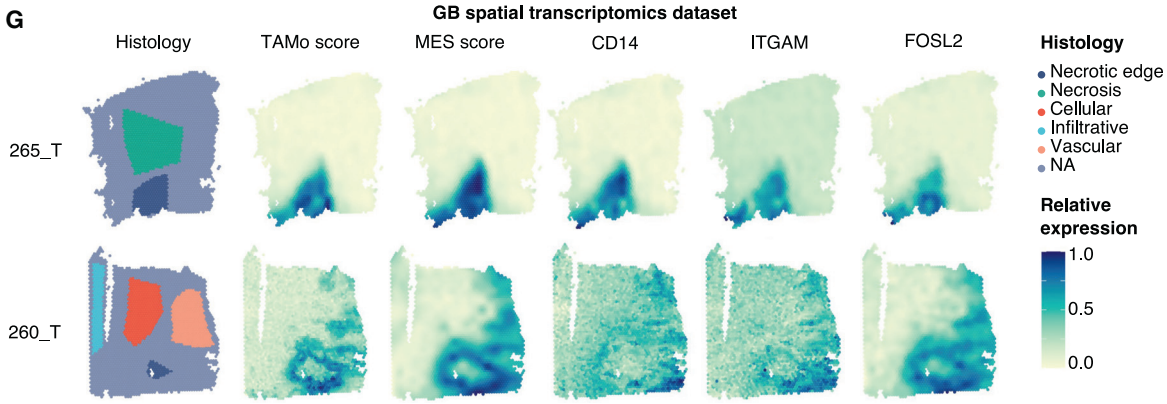

(legend on next page)

CellPress
OPEN ACCESS

which was defined as the TF regulon, were scored in individual cells. Regulon-based unbiased clustering robustly distinguished the TAMo population from PBMC-monocyte and MDM subgroups (Figure 5A), further supporting the distinctive cell identity of TAMo. Compared with PBMC-monocyte and MDM subgroups with high activity of well-known monocyte differentiation-related TF,[46] TAMo showed elevated activity of a set of TFs including *FOSL2*, *CEBPB*, *NFKB1*, *NFKB2*, and *NFIL3*. Apart from the inferred regulatory activity, several of these TFs also demonstrated significant over-expression in TAMo, especially *CEBPB* and *FOSL2* (Figure S5A). Interestingly, CEBPB and FOSL2 have been identified as the master regulators for mesenchymal GB,[34] and our analysis suggested their roles in reprogramming the glioma-infiltrating immune cells.

Examining the network regulated by CEBPB and FOSL2 in TAMo, we observed that FOSL2 positively regulated several TAMo signature genes, including *EREG* and *AREG* (Figures S5B and S5C). Moreover, among all potential TFs of *EREG* and *AREG*, FOSL2 was the top-ranked TF inferred by SCENIC (Figure 5B). The FOSL2 binding motifs were also detected in the two genes, and all FOSL2 ChIP-seq signal tracks available in the ENCODE portal[47,48] supported the binding of FOSL2 at these motif positions (Figure 5C). In the THP-1 monocyte cell line, the expression of EREG and AREG was significantly elevated and down-regulated in response to FOSL2 over-expression and knock-down, respectively (Figures 5D and 5E).[43] Overall, our analysis revealed CEBPB and FOSL2 as TAMo-specific master regulators, and, among these two important TFs, CEBPB was the upstream activator for FOSL2,[49] which further acted as the direct regulator for *EREG* and *AREG* expression in TAMo.

A recent study revealed that FOSL2 expression is induced in hypoxic conditions,[43] hinting the association between TAMo formation and necrosis, which is one of the histological hallmarks of a grade IV tumor diagnosis.[50] In the Ivy Glioblastoma Atlas Project (Ivy GAP) dataset with various anatomical regions of glioma,[51] we observed enrichment of TAMo near necrotic regions (Figure 5F). In contrast, enrichment of MG was observed in tumor periphery, while monocyte and MDM were preferentially localized at the regions with microvascular formation (Figure S5D), which is consistent with previous studies.[11,12] The spatial transcriptome dataset of IDH-wildtype GB[52] also revealed co-localization of the mesenchymal markers and TAMo, both of which were enriched near the necrotic edges (Figures 5G and S5E). In the two representative cases, all Mono/Macro (marked by CD14 and ITGAM) in tumor 265_T resembled the TAMo population and were found near the necrotic edge, while Mono/Macro were spatially dispersed in tumor 260_T and only the necrosis-proximal Mono/Macro resembled TAMo, suggesting that hypoxic environment at tumor necrosis areas may play a role in reprogramming infiltrating monocytes into TAMo. Interestingly, the enrichment of MHC-II-low monocytes at hypoxic areas, which tuned the expression of gene signatures related to angiogenesis and metastasis in these monocytes, was also reported in mouse models with lung and breast cancer.[53]

In vitro 3D spheroid model establishes the causal role of EREG and AREG in promoting GB cell invasion

We then modeled TAMo formation and TAMo-tumor interactions *in vitro*. Upon surveying 30 GB cell lines with available genomic and transcriptomic sequencing data in the Cancer Cell Line Encyclopedia database, we selected the U251 cell line as a GB cell model as it has an IDH-wildtype and EGFR-wildtype genomic background, as well as low expression in EREG and AREG (Figure S6A). To investigate the roles of EGFR-EREG/AREG axis in EGFR signaling and aggressive phenotypes in GB cells, trans-well invasion assay was used to evaluate the migration and invasion ability of U251 (Figures 6A and 6B). As a result, the invasion of U251 cells increased more than 2-fold with the addition of AREG and EREG (200 ng/mL) in the medium. Moreover, adding the EGFR inhibitor gefitinib in the medium notably decreased the invasion, demonstrating the role of EGFR signaling in regulating U251 cell invasion (Figures 6A, first row, and 6B, statistical analysis). Introducing human monocyte cell line THP-1 to the lower chamber of trans-well system stimulated the invasion of U251 cells cross the upper chamber, and the invasion positively correlated with the ratio of THP-1 cells in the non-contacting co-culture system (Figure 6A, second row).

To characterize the role of FOSL2, THP-1 cells with different expression levels of FOSL2 and AREG were developed. FOSL2 over-expression in THP-1 cells dramatically increased the invasion of U251 cross the trans-well chamber by approximately 2.8-fold (Figures 6A, third row, and 6B, 10th bar). In sharp contrast, the invasion significantly decreased when FOSL2 or AREG in THP-1 cells were downregulated (Figures 6A, third row, and 6B, eighth and ninth bars). Similar effects were observed when U251 cells were incubated with only THP-1 conditioned mediums instead of the cells, indicating FOSL2 is a master regulator in monocytes that mediates extracellular

Figure 5. TF activity analysis reveals FOSL2 as a regulator of TAMo

(A) Heatmap of TF activity inferred by SCENIC. Each row represented the regulon of one TF, and each column represented one monocyte or MDM profiled by 10X. The cell subcluster and tissue of origin were marked on top of the heatmap.

(B) The rank of feature importance scores of all TFs that potentially regulate *EREG* (top) and *AREG* expression (bottom). The dot size correlated with the importance of each TF, and the color represented whether the TF was over-expressed in GBM-infiltrating monocytes.

(C) The presence of FOSL2-binding peaks and motifs located near EREG (left) and AREG (right) genes. The data was obtained from ENCODE data portal.

(D and E) Expression levels of EREG and AREG in THP-1 monocyte cell line under FOSL2 over-expression (OE) (D) and knock-down (KD) (E) quantified by RT-PCR. ***$p < 0.001$, ****$p < 0.0001$ by two-sided unpaired t-test.

(F) Boxplot of TAMo score across different anatomical regions in IvyGBM dataset. p values were calculated by Wilcoxon rank-sum test and between the highest group versus other samples.

(G) Spatial distribution of Mono/Macro markers (CD14, ITGAM), FOSL2, TAMo score, and mesenchymal score across different histological regions in two IDH-wildtype GB patients. Abbreviations: PNZ, perinecrotic zone; PAN, pseudo-palisading cells around necrosis; MVP, microvascular proliferation; HBV, hyperplastic blood vessels; CT, cellular tumor; IT, infiltrating tumor; LE, leading edge.

See also Figure S5.

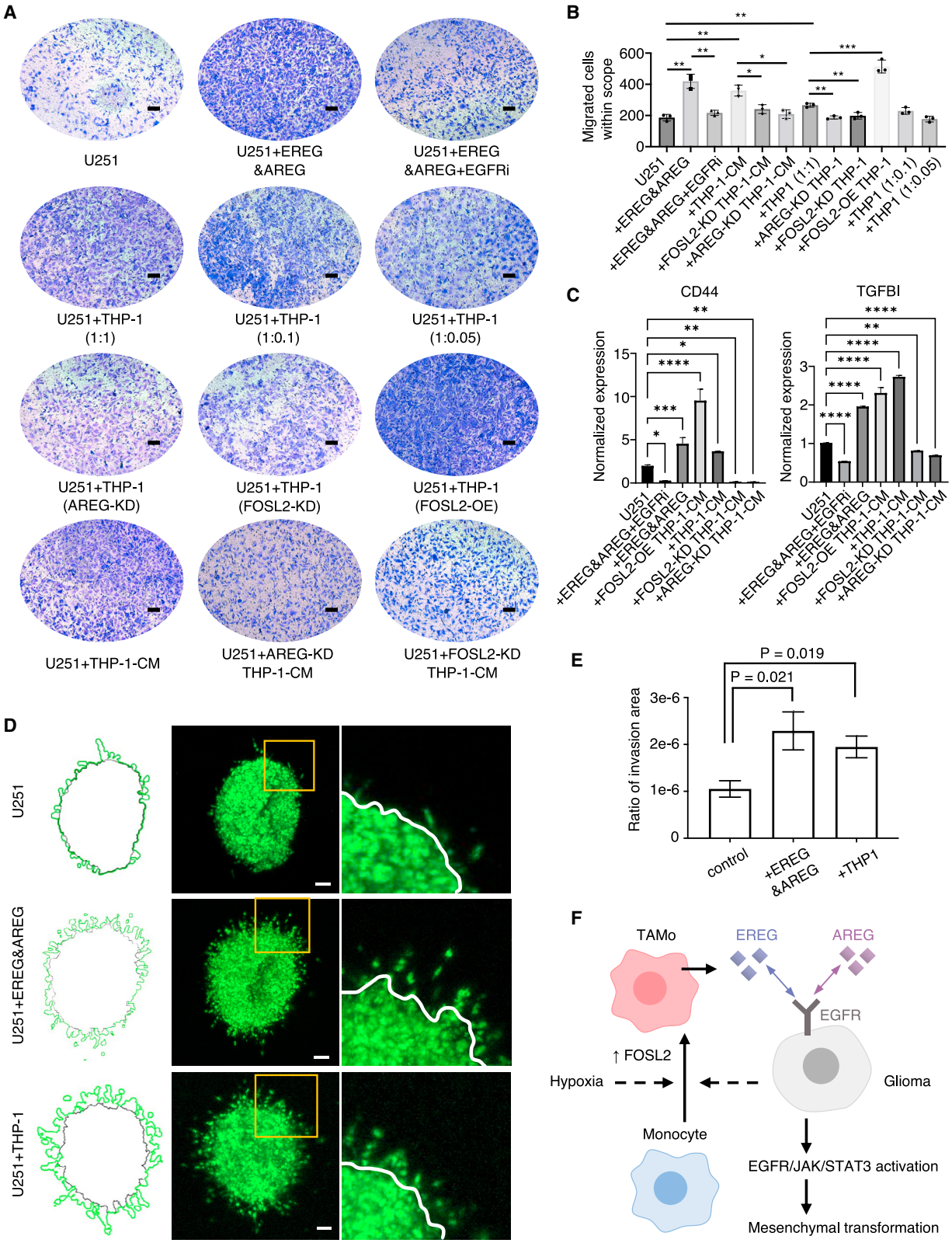

(legend on next page)

CellPress
OPEN ACCESS

signaling and promote GB cell invasion (Figures 6A, fourth row, and 6B, fourth and sixth bars). Moreover, the expression of mesenchymal markers (CD44 and TGFBI) in U251 cells showed consistent changes with invasiveness (Figure 6C), supporting the roles of FOSL2-EREG/AREG-EGFR axis in promoting the mesenchymal transformation of GB cells. Intriguingly, the THP-1 cells co-cultured with GB cell lines U251 or U87 also showed elevated expression of AREG and EREG (Figure S6B), thus suggesting reciprocal regulatory relationships between monocytes and GB.

To further visualize and evaluate tumor cell invasion, we developed a 3D culture system to mimic tumor microenvironmental conditions and monitor the tumor invasion process. By tracing the area of invasion in the high-resolution and 3D-stacked confocal images of U251 cell spheroids, the assay could robustly and quantitatively reflect differences in the invasion capabilities of the GB cells under different treatments. In the presence of EREG and AREG, the invasion of U251 cell spheroids drastically increased compared with the control (Figures 6D and S6C). The edge of the spheroid appeared more rugged due to profound cell invasion when EREG and AREG were included in the medium. Consistently, enhanced invasion of U251 cells were observed with inclusion of THP-1 into the culture system (Figures 6D and S6D). Quantification of the ratio of invasion area of U251 cell spheroids showed that both the presence of recombinant EREG and AREG proteins and the inclusion of THP-1 monocyte cells lead to significant increase in GB cell invasion (Figure 6E).

Altogether our study identified a group of prognosis-related, necrosis-associated, monocyte-derived cells called TAMo that was transcriptionally reprogrammed by FOSL2 to express EREG and AREG, which acts on GB tumor cells and promotes EGFR signaling and mesenchymal transformation (Figure 6F). The discovery of the FOSL2-EREG/AREG-EGFR axis in TAMo-tumor crosstalk will shed light on the design of next-generation immunotherapeutic strategies in GB.

DISCUSSION

We profiled the GB microenvironment, revealing changes in cell type abundance and transcriptional profiles. By combining scRNA-seq and CyTOF, our study sought to reveal GB-specific immune microenvironment features and mechanisms of tumor-immune interactions. Based on ontogeny-specific markers,[11] Mono/Macro could be classified into MG, MDM and monocytes. More important, GB-infiltrating monocytes, which we here termed TAMo, displayed elevated expression of EGFR ligands EREG and AREG, which were not expressed in PBMC-monocyte or MDM. The functions of EREG and AREG in activating EGFR signaling and promoting tumor growth, metastasis and vessel formation have already been well established in various cancer types.[54–57] By analyzing RNA-seq data of cross-sectional, longitudinal, and multicentric glioma samples, as well as spatial transcriptome dataset, we observed a consistent trend of mesenchymal transformation accompanied by TAMo infiltration. The presence of EREG and AREG also activated EGFR signaling, promoted the expression of mesenchymal markers, and enhanced GB cell invasion in trans-well invasion assays and 3D spheroid models.

TAMo and MDM both originate in bone marrow, but they have not been well distinguished in previous studies.[12,15] In the present study, the monocytes from PBMC were included in the clustering analysis and aided the discovery of TAMo that stably co-clustered with monocytes in PBMC. This co-clustering suggests that TAMo is more similar to monocyte, as opposed to differentiated macrophage states. The inclusion of PBMC-monocyte as a control may also provide a reasonable starting point for trajectory inference analysis. In another independent cohort, *EREG*- and *AREG*-expressing monocytes were defined as transitory macrophages that eventually differentiate into mature macrophages.[15] In contrast, with the addition of PBMC-monocyte as a starting point, we reconstructed the GB-infiltrating monocytes as a distinct terminal state of differentiation.

We hypothesized that monocytes undergo reprogramming initiated by the glioma cells after infiltrating into GB, resulting in the expression of TAMo-specific genes including *EREG* and *AREG*. Tumor-induced expression of EREG and AREG in monocytes has been reported in several breast cancer studies,[58,59] but the underlying mechanisms remain elusive. Through reconstructing TF regulons and comparing their activities in different Mono/Macro subgroups, we predicted and later verified the roles of FOSL2 in regulating EREG and AREG expression in TAMo. Enrichment of TAMo and FOSL2 expression near necrotic area also hinted the involvement of hypoxia and other GB-derived signaling molecules, such as extracellular ATP,[60] in

Figure 6. TAMo promotes glioma invasion via the FOSL2-EREG/AREG-EGFR axis

(A) Representative images of GB U251 cell in trans-well invasion assay under different treatment conditions. Scale bar, 100 μm. Abbreviations: CM, conditioned medium; EGFRi, EGFR inhibitor gefitinib.

(B) Quantification of U251 invasiveness in the trans-well invasion assay. Data were presented as mean ± SD (n = 3 biological replicates). p values were calculated by two-sided unpaired t-test. *$p < 0.05$, **$p < 0.01$, ***$p < 0.001$, ****$p < 0.0001$.

(C) Quantification of mesenchymal markers including CD44 and TGFBI in U251 cells under different treatment conditions using RT-PCR assay (n = 4 biological replicates).

(D) Representative images of GB U251 cell spheroid invasion 24 h after embedding in extracellular matrix with and without AREG and EREG treatment. From left to right: contour of the core (black lines) and invading protrusion of spheroids (green lines); raw images of spheroids, with the yellow squares representing the regions selected and zoomed in; zoomed view of spheroids, with white lines indicating the boundary between spheroid core and invading protrusion. Scale bar, 100 μm.

(E) Quantification of GB cell invasion from spheroids. Ratio of invasion area represents the ratio of the protrusion area over the core area of each spheroid (n = 2 biological replicates for control and n = 3 biological replicates for other groups).

(F) Proposed model of glioma- and/or hypoxia-mediated monocyte reprogramming into TAMo, which acted through the FOSL2-EREG/AREG-EGFR signaling axis and promoted mesenchymal transformation in glioma cells.

See also Figure S6.

driving the monocyte-TAMo transition. Other than the hypoxic microenvironment, elevated EREG and AREG expression was also observed in THP-1 co-cultured with GB cell lines, and this co-culture model could guide future studies of the molecular basis and mechanisms of extracellular signaling cues in GB that promote the transformation of monocytes into TAMo.

GB-infiltrating MDM and MG both showed elevated expression of TREM2 and CSF1R, which could be specifically targeted by anti-TREM2 and anti-CSF1R therapy. However, these strategies failed to deplete the GB-infiltrating monocytes in a recent study using a mouse model.[15] We observed lower levels of TREM2 and CSF1R expression in TAMo compared with MDM, which potentially resulted in the limited targeting efficiency on these cell populations. Alternatively, we identified a set of TAMo-specific markers, including EREG and AREG, that demonstrated low expression in PBMC-monocytes and MDM, which could be potentially targeted to eliminate TAMo without affecting the normal monocyte populations. The EREG- or AREG-blocking strategies also demonstrated effective tumor suppression in various cancer types.[61–63] Our study therefore lays the foundation for the future development of TAMo-targeted immunotherapy in glioma.

Taken together, our findings provide a comprehensive view of immune cell types in the GB microenvironment. We profiled the glioma and PBMC samples collected from the same patient using two single-cell profiling approaches, which complimented each other and generated useful data resources for glioma microenvironment studies. Significantly, this study reveal TAMo as a key player in promoting EGFR signaling and mesenchymal transformation in glioma. For future perspectives, our study will serve as a useful reference for enhancing the understanding of the tumor microenvironment for rational design and improvement of immunotherapy in GB.

Limitations of the study

While our study computationally and experimentally studied the TAMo-glioma interactions *in vitro*, further efforts should be devoted to establishing better *in vitro* and *in vivo* systems to study this phenomenon. The *in vitro* experiments in this study were carried out in long-term cultured cancer and monocyte cell lines, while patient-derived glioma stem cells and primary peripheral blood monocytes could more faithfully recapitulate glioma and monocytes. Second, while our study verified the roles of TAMo in promoting mesenchymal transformation of the tumor, the possibility of positive regulatory loops between TAMo and mesenchymal GB also need to be anticipated and examined. Lastly, the clinical implications and translational potentials of our findings require further mechanistic studies and validation in larger patient cohorts.

STAR★METHODS

Detailed methods are provided in the online version of this paper and include the following:

- KEY RESOURCES TABLE
- RESOURCE AVAILABILITY
  - Lead contact
  - Materials availability
  - Data and code availability
- EXPERIMENTAL MODEL AND SUBJECT DETAILS
  - Patients and ethics statements
  - Cell culture
- METHOD DETAILS
  - GB specimens single-cell dissociation
  - Peripheral blood single-cell dissociation
  - Mass cytometry
  - Single-cell RNA sequencing
  - CyTOF data analysis
  - Analysis of single-cell RNA sequencing data
  - Single-cell trajectory analysis
  - Identifying Mono/Macro subtypes
  - Differential expression and pathway activity analysis
  - Scoring MG, MDM, monocyte and TAMo abundance in bulk RNA sequencing data
  - Survival analysis
  - Scoring mesenchymal transformation in paired samples from the same patient
  - Single-cell transcriptional network analysis
  - Glioblastoma proteomic data analysis
  - Glioblastoma spatial transcriptome data analysis
  - siRNA transfection and reverse transcription-PCR
  - Trans-well invasion assay
  - 3D spheroid invasion assay
  - Immunofluorescence staining
- QUANTIFICATION AND STATISTICAL ANALYSIS

SUPPLEMENTAL INFORMATION

Supplemental information can be found online at https://doi.org/10.1016/j.xcrm.2023.101177.

ACKNOWLEDGMENTS

This work was supported by National Natural Science Foundation of China (31922088, 82192894) and Mainland (MOST)-Hong Kong (ITC) Joint Funding Scheme (No. 2019YFE0109400 to Jiang lab, No. MHP/004/19 to Wang lab), RGC grants (16101021, 26102719, 27115220, CRS_HKUST605/22, and R6003-22), ITC grant (ITCPD/17-9), and grant from Department of Science and Technology of Guangdong Province (No. 2020A0505090007). This work was supported in part by the Project of Hetao Shenzhen-Hong Kong Science and Technology Innovation Cooperation Zone (HZQB-KCZYB-2020083). J.W. is supported by Padma Harilela Professorship. We thank Dr Chan Chi Ping at the School of Biomedical Sciences, The University of Hong Kong for providing THP-1 cells, and Dr Hin Chu at the Department of Microbiology, The University of Hong Kong for providing U251 cells. We acknowledge The University of Hong Kong, Li Ka Shing Faculty of Medicine Core Facility for assistance.

AUTHOR CONTRIBUTIONS

Conceptualization, J.W. and Y.Cao; formal analysis, Y.Chen, W.F., R.M., Z.Zhu, X.Z., and J.T.; investigation, R.H., W.K., Y.L., Q.L., Y.H., M.Y., and R.C.; resources, R.H., W.F., T.J., and Y.Cao; data curation, B.J., Z.B., and Z.Zhao; writing – original draft, Y.Chen, W.K., and J.W.; writing – review and editing, Y.Chen, W.K., Z.Zhao, Z.H., and J.W.; supervision, W.W., T.J., Y.Cao, and J.W.; funding acquisition, W.W., T.J., Y.Cao, and J.W.

DECLARATION OF INTERESTS

The authors declare no competing interests.

Received: August 2, 2022
Revised: March 12, 2023
Accepted: August 9, 2023
Published: August 30, 2023

REFERENCES

1. Stupp, R., Mason, W.P., van den Bent, M.J., Weller, M., Fisher, B., Taphoorn, M.J.B., Belanger, K., Brandes, A.A., Marosi, C., Bogdahn, U., et al. (2005). Radiotherapy plus Concomitant and Adjuvant Temozolomide for Glioblastoma. N. Engl. J. Med. *352*, 987–996. https://doi.org/10.1056/NEJMoa043330.
2. Cloughesy, T.F., Mochizuki, A.Y., Orpilla, J.R., Hugo, W., Lee, A.H., Davidson, T.B., Wang, A.C., Ellingson, B.M., Rytlewski, J.A., Sanders, C.M., et al. (2019). Neoadjuvant anti-PD-1 immunotherapy promotes a survival benefit with intratumoral and systemic immune responses in recurrent glioblastoma. Nat. Med. *25*, 477–486. https://doi.org/10.1038/s41591-018-0337-7.
3. Keskin, D.B., Anandappa, A.J., Sun, J., Tirosh, I., Mathewson, N.D., Li, S., Oliveira, G., Giobbie-Hurder, A., Felt, K., Gjini, E., et al. (2019). Neoantigen vaccine generates intratumoral T cell responses in phase Ib glioblastoma trial. Nature *565*, 234–239. https://doi.org/10.1038/s41586-018-0792-9.
4. McGranahan, T., Therkelsen, K.E., Ahmad, S., and Nagpal, S. (2019). Current State of Immunotherapy for Treatment of Glioblastoma. Curr. Treat. Options Oncol. *20*, 24. https://doi.org/10.1007/s11864-019-0619-4.
5. De Groot, J., Penas-Prado, M., Alfaro-Munoz, K., Hunter, K., Pei, B.L., O'Brien, B., Weathers, S.P., Loghin, M., Kamiya Matsouka, C., Yung, W.K.A., et al. (2020). Window-of-opportunity clinical trial of pembrolizumab in patients with recurrent glioblastoma reveals predominance of immune-suppressive macrophages. Neuro Oncol. *22*, 539–549. https://doi.org/10.1093/neuonc/noz185.
6. Pyonteck, S.M., Akkari, L., Schuhmacher, A.J., Bowman, R.L., Sevenich, L., Quail, D.F., Olson, O.C., Quick, M.L., Huse, J.T., Teijeiro, V., et al. (2013). CSF-1R inhibition alters macrophage polarization and blocks glioma progression. Nat. Med. *19*, 1264–1272. https://doi.org/10.1038/nm.3337.
7. Butowski, N., Colman, H., De Groot, J.F., Omuro, A.M., Nayak, L., Wen, P.Y., Cloughesy, T.F., Marimuthu, A., Haidar, S., Perry, A., et al. (2016). Orally administered colony stimulating factor 1 receptor inhibitor PLX3397 in recurrent glioblastoma: An Ivy Foundation Early Phase Clinical Trials Consortium phase II study. Neuro Oncol. *18*, 557–564. https://doi.org/10.1093/neuonc/nov245.
8. Mu, Q., Chen, Y., and Wang, J. (2019). Deciphering Brain Complexity Using Single-cell Sequencing. Dev. Reprod. Biol. *17*, 344–366. https://doi.org/10.1016/j.gpb.2018.07.007.
9. Venteicher, A.S., Tirosh, I., Hebert, C., Yizhak, K., Neftel, C., Filbin, M.G., Hovestadt, V., Escalante, L.E., Shaw, M.L., Rodman, C., et al. (2017). Decoupling genetics, lineages, and microenvironment in IDH-mutant gliomas by single-cell RNA-seq. Science *355*, eaai8478. https://doi.org/10.1126/science.aai8478.
10. Darmanis, S., Sloan, S.A., Croote, D., Mignardi, M., Chernikova, S., Samghababi, P., Zhang, Y., Neff, N., Kowarsky, M., Caneda, C., et al. (2017). Single-cell RNA-seq analysis of infiltrating neoplastic cells at the migrating front of human glioblastoma. Cell Rep. *21*, 1399–1410. https://doi.org/10.1016/j.celrep.2017.10.030.
11. Müller, S., Kohanbash, G., Liu, S.J., Alvarado, B., Carrera, D., Bhaduri, A., Watchmaker, P.B., Yagnik, G., di Lullo, E., Malatesta, M., et al. (2017). Single-cell profiling of human gliomas reveals macrophage ontogeny as a basis for regional differences in macrophage activation in the tumor microenvironment. Genome Biol. *18*, 1–14. https://doi.org/10.1186/s13059-017-1362-4.
12. Friebel, E., Kapolou, K., Unger, S., Núñez, N.G., Utz, S., Rushing, E.J., Regli, L., Weller, M., Greter, M., Tugues, S., et al. (2020). Single-Cell Mapping of Human Brain Cancer Reveals Tumor-Specific Instruction of Tissue-Invading Leukocytes. Cell *181*, 1626–1642.e20. https://doi.org/10.1016/j.cell.2020.04.055.
13. Sankowski, R., Böttcher, C., Masuda, T., Geirsdottir, L., Sagar, Sindram, E., Sindram, E., Seredenina, T., Muhs, A., Scheiwe, C., Shah, M.J., et al. (2019). Mapping microglia states in the human brain through the integration of high-dimensional techniques. Nat. Neurosci. *22*, 2098–2110. https://doi.org/10.1038/s41593-019-0532-y.
14. Goswami, S., Walle, T., Cornish, A.E., Basu, S., Anandhan, S., Fernandez, I., Vence, L., Blando, J., Zhao, H., Yadav, S.S., et al. (2020). Immune profiling of human tumors identifies CD73 as a combinatorial target in glioblastoma. Nat. Med. *26*, 39–46. https://doi.org/10.1038/s41591-019-0694-x.
15. Pombo Antunes, A.R., Scheyltjens, I., Lodi, F., Messiaen, J., Antoranz, A., Duerinck, J., Kancheva, D., Martens, L., de Vlaminck, K., van Hove, H., et al. (2021). Single-cell profiling of myeloid cells in glioblastoma across species and disease stage reveals macrophage competition and specialization. Nat. Neurosci. *24*, 595–610. https://doi.org/10.1038/s41593-020-00789-y.
16. Verhaak, R.G.W., Hoadley, K.A., Purdom, E., Wang, V., Qi, Y., Wilkerson, M.D., Miller, C.R., Ding, L., Golub, T., Mesirov, J.P., et al. (2010). Integrated Genomic Analysis Identifies Clinically Relevant Subtypes of Glioblastoma Characterized by Abnormalities in PDGFRA, IDH1, EGFR, and NF1. Cancer Cell *17*, 98–110. https://doi.org/10.1016/j.ccr.2009.12.020.
17. Maecker, H.T., McCoy, J.P., and Nussenblatt, R. (2012). Standardizing immunophenotyping for the Human Immunology Project. Nat. Rev. Immunol. *12*, 191–200. https://doi.org/10.1038/nri3158.
18. Aran, D., Looney, A.P., Liu, L., Wu, E., Fong, V., Hsu, A., Chak, S., Naikawadi, R.P., Wolters, P.J., Abate, A.R., et al. (2019). Reference-based analysis of lung single-cell sequencing reveals a transitional profibrotic macrophage. Nat. Immunol. *20*, 163–172. https://doi.org/10.1038/s41590-018-0276-y.
19. Martin, M.D., and Badovinac, V.P. (2018). Defining memory CD8 T cell. Front. Immunol. *9*, 2692. https://doi.org/10.3389/fimmu.2018.02692.
20. Chen, Y., Zander, R., Khatun, A., Schauder, D.M., and Cui, W. (2018). Transcriptional and Epigenetic Regulation of Effector and Memory CD8 T Cell Differentiation. Front. Immunol. *9*, 2826. https://doi.org/10.3389/fimmu.2018.02826.
21. Poli, A., Michel, T., Thérésine, M., Andrès, E., Hentges, F., and Zimmer, J. (2009). CD56bright natural killer (NK) cells: An important NK cell subset. Immunology *126*, 458–465. https://doi.org/10.1111/j.1365-2567.2008.03027.x.
22. Close, H.J., Stead, L.F., Nsengimana, J., Reilly, K.A., Droop, A., Wurdak, H., Mathew, R.K., Corns, R., Newton-Bishop, J., Melcher, A.A., et al. (2020). Expression profiling of single cells and patient cohorts identifies multiple immunosuppressive pathways and an altered NK cell phenotype in glioblastoma. Clin. Exp. Immunol. *200*, 33–44. https://doi.org/10.1111/CEI.13403.
23. Carrega, P., Morandi, B., Costa, R., Ferlazzo, G., Frumento, G., Altavilla, G., Ratto, G.B., Mingari, M.C., Moretta, L., and Forte, G. (2008). Natural killer cells infiltrating human nonsmall-cell lung cancer are enriched in CD56 bright CD16(-) cells and display an impaired capability to kill tumor cells. Cancer *112*, 863–875. https://doi.org/10.1002/CNCR.23239.
24. André, P., Denis, C., Soulas, C., Bourbon-Caillet, C., Lopez, J., Arnoux, T., Bléry, M., Bonnafous, C., Gauthier, L., Morel, A., et al. (2018). Anti-NKG2A mAb Is a Checkpoint Inhibitor that Promotes Anti-tumor Immunity by Unleashing Both T and NK Cells. Cell *175*, 1731–1743.e13. https://doi.org/10.1016/J.CELL.2018.10.014.
25. Kamiya, T., Seow, S.V., Wong, D., Robinson, M., and Campana, D. (2019). Blocking expression of inhibitory receptor NKG2A overcomes tumor resistance to NK cells. J. Clin. Invest. *129*, 2094–2106. https://doi.org/10.1172/JCI123955.
26. Klemm, F., Maas, R.R., Bowman, R.L., Kornete, M., Soukup, K., Nassiri, S., Brouland, J.P., Iacobuzio-Donahue, C.A., Brennan, C., Tabar, V., et al. (2020). Interrogation of the Microenvironmental Landscape in Brain

Tumors Reveals Disease-Specific Alterations of Immune Cells. Cell *181*, 1643–1660.e17. https://doi.org/10.1016/j.cell.2020.05.007.

27. Chen, A.X., Gartrell, R.D., Zhao, J., Upadhyayula, P.S., Zhao, W., Yuan, J., Minns, H.E., Dovas, A., Bruce, J.N., Lasorella, A., et al. (2021). Single-cell characterization of macrophages in glioblastoma reveals MARCO as a mesenchymal pro-tumor marker. Genome Med. *13*, 88–13. https://doi.org/10.1186/S13073-021-00906-X/FIGURES/5.
28. Zhao, J., Chen, A.X., Gartrell, R.D., Silverman, A.M., Aparicio, L., Chu, T., Bordbar, D., Shan, D., Samanamud, J., Mahajan, A., et al. (2019). Immune and genomic correlates of response to anti-PD-1 immunotherapy in glioblastoma. Nat. Med. *25*, 462–469. https://doi.org/10.1038/s41591-019-0349-y.
29. Cassetta, L., and Pollard, J.W. (2018). Targeting macrophages: Therapeutic approaches in cancer. Nat. Rev. Drug Discov. *17*, 887–904. https://doi.org/10.1038/nrd.2018.169.
30. Zhao, Z., Meng, F., Wang, W., Wang, Z., Zhang, C., and Jiang, T. (2017). Comprehensive RNA-seq transcriptomic profiling in the malignant progression of gliomas. Sci. Data *4*, 170024. https://doi.org/10.1038/SDATA.2017.24.
31. Zhao, Z., Zhang, K.N., Wang, Q., Li, G., Zeng, F., Zhang, Y., Wu, F., Chai, R., Wang, Z., Zhang, C., et al. (2021). Chinese Glioma Genome Atlas (CGGA): A Comprehensive Resource with Functional Genomic Data from Chinese Glioma Patients. Dev. Reprod. Biol. *19*, 1–12. https://doi.org/10.1016/J.GPB.2020.10.005.
32. Chen, P., Zhao, D., Li, J., Liang, X., Li, J., Chang, A., Henry, V.K., Lan, Z., Spring, D.J., Rao, G., et al. (2019). Symbiotic Macrophage-Glioma Cell Interactions Reveal Synthetic Lethality in PTEN-Null Glioma. Cancer Cell *35*, 868–884.e6. https://doi.org/10.1016/J.CCELL.2019.05.003.
33. Ni, X., Wu, W., Sun, X., Ma, J., Yu, Z., He, X., Cheng, J., Xu, P., Liu, H., Shang, T., et al. (2022). Interrogating glioma-M2 macrophage interactions identifies Gal-9/Tim-3 as a viable target against PTEN-null glioblastoma. Sci. Adv. *8*, 5165. https://doi.org/10.1126/SCIADV.ABL5165/SUPPL_FILE/SCIADV.ABL5165_SM.PDF.
34. Carro, M.S., Lim, W.K., Alvarez, M.J., Bollo, R.J., Zhao, X., Snyder, E.Y., Sulman, E.P., Anne, S.L., Doetsch, F., Colman, H., et al. (2009). The transcriptional network for mesenchymal transformation of brain tumours. Nature *463*, 318–325. https://doi.org/10.1038/nature08712.
35. Wang, L.B., Karpova, A., Gritsenko, M.A., Kyle, J.E., Cao, S., Li, Y., Rykunov, D., Colaprico, A., Rothstein, J.H., Hong, R., et al. (2021). Proteogenomic and metabolomic characterization of human glioblastoma. Cancer Cell *39*, 509–528.e20. https://doi.org/10.1016/J.CCELL.2021.01.006.
36. Wang, J., Cazzato, E., Ladewig, E., Frattini, V., Rosenbloom, D.I.S., Zairis, S., Abate, F., Liu, Z., Elliott, O., Shin, Y.-J., et al. (2016). Clonal evolution of glioblastoma under therapy. Nat. Genet. *48*, 768–776. https://doi.org/10.1038/ng.3590.
37. Lee, J.K., Wang, J., Sa, J.K., Ladewig, E., Lee, H.-O., Lee, I.-H., Kang, H.J., Rosenbloom, D.S., Camara, P.G., Liu, Z., et al. (2017). Spatiotemporal genomic architecture informs precision oncology in glioblastoma. Nat. Genet. *49*, 594–599. https://doi.org/10.1038/ng.3806.
38. Hu, H., Mu, Q., Bao, Z., Chen, Y., Liu, Y., Chen, J., Wang, K., Wang, Z., Nam, Y., Jiang, B., et al. (2018). Mutational Landscape of Secondary Glioblastoma Guides MET-Targeted Trial in Brain Tumor. Cell *175*, 1665–1678.e18. https://doi.org/10.1016/j.cell.2018.09.038.
39. Wang, Q., Hu, B., Hu, X., Kim, H., Squatrito, M., Scarpace, L., DeCarvalho, A.C., Lyu, S., Li, P., Li, Y., et al. (2017). Tumor evolution of glioma-intrinsic gene expression subtypes associates with immunological changes in the microenvironment. Cancer Cell *32*, 42–56.e6. https://doi.org/10.1016/J.CCELL.2017.06.003.
40. Kim, Y., Varn, F.S., Park, S.H., Yoon, B.W., Park, H.R., Lee, C., Verhaak, R.G.W., and Paek, S.H. (2021). Perspective of mesenchymal transformation in glioblastoma. Acta Neuropathol. Commun. *9*, 50. https://doi.org/10.1186/S40478-021-01151-4.
41. Hara, T., Chanoch-Myers, R., Mathewson, N.D., Myskiw, C., Atta, L., Bussema, L., Eichhorn, S.W., Greenwald, A.C., Kinker, G.S., Rodman, C., et al. (2021). Interactions between cancer cells and immune cells drive transitions to mesenchymal-like states in glioblastoma. Cancer Cell *39*, 779–792.e11. https://doi.org/10.1016/J.CCELL.2021.05.002.
42. Sa, J.K., Chang, N., Lee, H.W., Cho, H.J., Ceccarelli, M., Cerulo, L., Yin, J., Kim, S.S., Caruso, F.P., Lee, M., et al. (2020). Transcriptional regulatory networks of tumor-associated macrophages that drive malignancy in mesenchymal glioblastoma. Genome Biol. *21*, 216. https://doi.org/10.1186/s13059-020-02140-x.
43. Wu, L., Wu, W., Zhang, J., Zhao, Z., Li, L., Zhu, M., Wu, M., Wu, F., Zhou, F., Du, Y., et al. (2022). Natural Coevolution of Tumor and Immunoenvironment in Glioblastoma. Cancer Discov. *12*, 2820–2837. https://doi.org/10.1158/2159-8290.CD-22-0196/709256/AM/NATURAL-.
44. Neftel, C., Laffy, J., Filbin, M.G., Hara, T., Shore, M.E., Rahme, G.J., Richman, A.R., Silverbush, D., Shaw, M.L., Hebert, C.M., et al. (2019). An integrative model of cellular states, plasticity, and genetics for glioblastoma. Cell *178*, 835–849.e21. https://doi.org/10.1016/J.CELL.2019.06.024.
45. Aibar, S., González-Blas, C.B., Moerman, T., Huynh-Thu, V.A., Imrichova, H., Hulselmans, G., Rambow, F., Marine, J.C., Geurts, P., Aerts, J., et al. (2017). SCENIC: Single-cell regulatory network inference and clustering. Nat. Methods *14*, 1083–1086. https://doi.org/10.1038/nmeth.4463.
46. Huber, R., Pietsch, D., Günther, J., Welz, B., Vogt, N., and Brand, K. (2014). Regulation of monocyte differentiation by specific signaling modules and associated transcription factor networks. Cell. Mol. Life Sci. *71*, 63–92. https://doi.org/10.1007/S00018-013-1322-4/FIGURES/3.
47. ENCODE Project Consortium (2012). An integrated encyclopedia of DNA elements in the human genome. Nature *489*, 57–74. https://doi.org/10.1038/nature11247.
48. Luo, Y., Hitz, B.C., Gabdank, I., Hilton, J.A., Kagda, M.S., Lam, B., Myers, Z., Sud, P., Jou, J., Lin, K., et al. (2020). New developments on the Encyclopedia of DNA Elements (ENCODE) data portal. Nucleic Acids Res. *48*, D882–D889. https://doi.org/10.1093/NAR/GKZ1062.
49. Carro, M.S., Lim, W.K., Alvarez, M.J., Bollo, R.J., Zhao, X., Snyder, E.Y., Sulman, E.P., Anne, S.L., Doetsch, F., Colman, H., et al. (2010). The transcriptional network for mesenchymal transformation of brain tumours. Nature *463*, 318–325. https://doi.org/10.1038/nature08712.
50. Weller, M., van den Bent, M., Preusser, M., le Rhun, E., Tonn, J.C., Minniti, G., Bendszus, M., Balana, C., Chinot, O., Dirven, L., et al. (2020). EANO guidelines on the diagnosis and treatment of diffuse gliomas of adulthood. Nat. Rev. Clin. Oncol. *18*, 170–186. https://doi.org/10.1038/s41571-020-00447-z.
51. Puchalski, R.B., Shah, N., Miller, J., Dalley, R., Nomura, S.R., Yoon, J.G., Smith, K.A., Lankerovich, M., Bertagnolli, D., Bickley, K., et al. (2018). An anatomic transcriptional atlas of human glioblastoma. Science *360*, 660–663. https://doi.org/10.1126/SCIENCE.AAF2666/SUPPL_FILE/AAF2666_TABLE-S9.XLSX.
52. Ravi, V.M., Will, P., Kueckelhaus, J., Sun, N., Joseph, K., Salié, H., Vollmer, L., Kuliesiute, U., von Ehr, J., Benotmane, J.K., et al. (2022). Spatially resolved multi-omics deciphers bidirectional tumor-host interdependence in glioblastoma. Cancer Cell *40*, 639–655.e13. https://doi.org/10.1016/J.CCELL.2022.05.009.
53. Henze, A.T., and Mazzone, M. (2016). The impact of hypoxia on tumor-associated macrophages. J. Clin. Invest. *126*, 3672–3679. https://doi.org/10.1172/JCI84427.
54. Kohsaka, S., Hinohara, K., Wang, L., Nishimura, T., Urushido, M., Yachi, K., Tsuda, M., Tanino, M., Kimura, T., Nishihara, H., et al. (2014). Epiregulin enhances tumorigenicity by activating the ERK/MAPK pathway in glioblastoma. Neuro Oncol. *16*, 960–970. https://doi.org/10.1093/NEUONC/NOT315.
55. Gupta, G.P., Nguyen, D.X., Chiang, A.C., Bos, P.D., Kim, J.Y., Nadal, C., Gomis, R.R., Manova-Todorova, K., and Massagué, J. (2007). Mediators of vascular remodelling co-opted for sequential steps in lung metastasis. Nature *446*, 765–770. https://doi.org/10.1038/nature05760.

56. Cheng, W.L., Feng, P.H., Lee, K.Y., Chen, K.Y., Sun, W.L., van Hiep, N., Luo, C.S., and Wu, S.M. (2021). The Role of EREG/EGFR Pathway in Tumor Progression. Int. J. Mol. Sci. *22*, 12828. https://doi.org/10.3390/IJMS222312828.

57. Busser, B., Sancey, L., Brambilla, E., Coll, J.L., and Hurbin, A. (2011). The multiple roles of amphiregulin in human cancer. Biochim. Biophys. Acta *1816*, 119–131. https://doi.org/10.1016/J.BBCAN.2011.05.003.

58. Vlaicu, P., Mertins, P., Mayr, T., Widschwendter, P., Ataseven, B., Högel, B., Eiermann, W., Knyazev, P., and Ullrich, A. (2013). Monocytes/macrophages support mammary tumor invasivity by co-secreting lineage-specific EGFR ligands and a STAT3 activator. BMC Cancer *13*, 197–213. https://doi.org/10.1186/1471-2407-13-197/FIGURES/5.

59. Sánchez-González, I., Bobien, A., Molnar, C., Schmid, S., Strotbek, M., Boerries, M., Busch, H., and Olayioye, M.A. (2020). miR-149 Suppresses Breast Cancer Metastasis by Blocking Paracrine Interactions with Macrophages. Cancer Res. *80*, 1330–1341. https://doi.org/10.1158/0008-5472.CAN-19-1934.

60. Bles, N., di Pietrantonio, L., Boeynaems, J.M., and Communi, D. (2010). ATP confers tumorigenic properties to dendritic cells by inducing amphiregulin secretion. Blood *116*, 3219–3226. https://doi.org/10.1182/BLOOD-2010-01-265611.

61. Carvalho, S., Lindzen, M., Lauriola, M., Shirazi, N., Sinha, S., Abdul-Hai, A., Levanon, K., Korach, J., Barshack, I., Cohen, Y., et al. (2016). An antibody to amphiregulin, an abundant growth factor in patients' fluids, inhibits ovarian tumors. Oncogene *35*, 438–447. https://doi.org/10.1038/onc.2015.93.

62. Zhang, J., Iwanaga, K., Choi, K.C., Wislez, M., Raso, M.G., Wei, W., Wistuba, I.I., and Kurie, J.M. (2008). Intratumoral epiregulin is a marker of advanced disease in non-small cell lung cancer patients and confers invasive properties on EGFR-mutant cells. Cancer Prev. Res. *1*, 201–207. https://doi.org/10.1158/1940-6207.CAPR-08-0014.

63. Iijima, M., Anai, M., Kodama, T., and Shibasaki, Y. (2017). Epiregulin-blocking antibody inhibits epiregulin-dependent EGFR signaling. Biochem. Biophys. Res. Commun. *489*, 83–88. https://doi.org/10.1016/J.BBRC.2017.03.006.

64. Stuart, T., Butler, A., Hoffman, P., Hafemeister, C., Papalexi, E., Mauck, W.M., Hao, Y., Stoeckius, M., Smibert, P., and Satija, R. (2019). Comprehensive Integration of Single-Cell Data. Cell *177*, 1888–1902.e21. https://doi.org/10.1016/j.cell.2019.05.031.

65. Patel, A.P., Tirosh, I., Trombetta, J.J., Shalek, A.K., Gillespie, S.M., Wakimoto, H., Cahill, D.P., Nahed, B.v., Curry, W.T., Martuza, R.L., et al. (2014). Single-cell RNA-seq highlights intratumoral heterogeneity in primary glioblastoma. Science *344*, 1396–1401. https://doi.org/10.1126/science.1254257.

66. Street, K., Risso, D., Fletcher, R.B., Das, D., Ngai, J., Yosef, N., Purdom, E., and Dudoit, S. (2018). Slingshot: cell lineage and pseudotime inference for single-cell transcriptomics. BMC Genom. *19*, 1–16. https://doi.org/10.1186/S12864-018-4772-0.

67. Trapnell, C., Cacchiarelli, D., Grimsby, J., Pokharel, P., Li, S., Morse, M., Lennon, N.J., Livak, K.J., Mikkelsen, T.S., and Rinn, J.L. (2014). The dynamics and regulators of cell fate decisions are revealed by pseudotemporal ordering of single cells. Nat. Biotechnol. *32*, 381–386. https://doi.org/10.1038/nbt.2859.

68. Qiu, X., Hill, A., Packer, J., Lin, D., Ma, Y.A., and Trapnell, C. (2017). Single-cell mRNA quantification and differential analysis with Census. Nat. Methods *14*, 309–315. https://doi.org/10.1038/nmeth.4150.

69. Qiu, X., Mao, Q., Tang, Y., Wang, L., Chawla, R., Pliner, H.A., and Trapnell, C. (2017). Reversed graph embedding resolves complex single-cell trajectories. Nat. Methods *14*, 979–982. https://doi.org/10.1038/nmeth.4402.

70. Cao, J., Spielmann, M., Qiu, X., Huang, X., Ibrahim, D.M., Hill, A.J., Zhang, F., Mundlos, S., Christiansen, L., Steemers, F.J., et al. (2019). The single-cell transcriptional landscape of mammalian organogenesis. Nature *566*, 496–502. https://doi.org/10.1038/s41586-019-0969-x.

71. Subramanian, A., Tamayo, P., Mootha, V.K., Mukherjee, S., Ebert, B.L., Gillette, M.A., Paulovich, A., Pomeroy, S.L., Golub, T.R., Lander, E.S., and Mesirov, J.P. (2005). Gene set enrichment analysis: a knowledge-based approach for interpreting genome-wide expression profiles. Proc. Natl. Acad. Sci. USA *102*, 15545–15550. https://doi.org/10.1073/pnas.0506580102.

72. Wilkerson, M.D., and Hayes, D.N. (2010). ConsensusClusterPlus: a class discovery tool with confidence assessments and item tracking. Bioinformatics *26*, 1572–1573. https://doi.org/10.1093/bioinformatics/btq170.

73. Davidson-Pilon, C. (2019). Lifelines: survival analysis in Python. Journal of Open Source Software *4*, 1317. https://doi.org/10.21105/joss.01317.

74. Finck, R., Simonds, E.F., Jager, A., Krishnaswamy, S., Sachs, K., Fantl, W., Pe'er, D., Nolan, G.P., and Bendall, S.C. (2013). Normalization of mass cytometry data with bead standards. Cytometry A. *83*, 483–494. https://doi.org/10.1002/cyto.a.22271.

75. Kotecha, N., Krutzik, P.O., and Irish, J.M. (2010). Web-based analysis and publication of flow cytometry experiments. Curr. Protoc. Cytom. *10*, 10.17, *Chapter 10*. https://doi.org/10.1002/0471142956.cy1017s53.

76. Korin, B., Ben-Shaanan, T.L., Schiller, M., Dubovik, T., Azulay-Debby, H., Boshnak, N.T., Koren, T., and Rolls, A. (2017). High-dimensional, single-cell characterization of the brain's immune compartment. Nat. Neurosci. *20*, 1300–1309. https://doi.org/10.1038/nn.4610.

77. Amir, E.A.D., Davis, K.L., Tadmor, M.D., Simonds, E.F., Levine, J.H., Bendall, S.C., Shenfeld, D.K., Krishnaswamy, S., Nolan, G.P., and Pe'Er, D. (2013). ViSNE enables visualization of high dimensional single-cell data and reveals phenotypic heterogeneity of leukemia. Nat. Biotechnol. *31*, 545–552. https://doi.org/10.1038/nbt.2594.

78. Zheng, G.X.Y., Terry, J.M., Belgrader, P., Ryvkin, P., Bent, Z.W., Wilson, R., Ziraldo, S.B., Wheeler, T.D., McDermott, G.P., Zhu, J., et al. (2017). Massively parallel digital transcriptional profiling of single cells. Nat. Commun. *8*, 14049. https://doi.org/10.1038/ncomms14049.

79. Brunet, J.P., Tamayo, P., Golub, T.R., and Mesirov, J.P. (2004). Metagenes and molecular pattern discovery using matrix factorization. Proc. Natl. Acad. Sci. USA *101*, 4164–4169. https://doi.org/10.1073/PNAS.0308531101/SUPPL_FILE/08531DATASET9.RTF.

80. Uhlen, M., Zhang, C., Lee, S., Sjöstedt, E., Fagerberg, L., Bidkhori, G., Benfeitas, R., Arif, M., Liu, Z., Edfors, F., et al. (2017). A pathology atlas of the human cancer transcriptome. Science *357*, eaan2507. https://doi.org/10.1126/science.aan2507.

81. Veelken, C., Bakker, G.J., Drell, D., and Friedl, P. (2017). Single cell-based automated quantification of therapy responses of invasive cancer spheroids in organotypic 3D culture. Methods *128*, 139–149. https://doi.org/10.1016/J.YMETH.2017.07.015.

82. Conti, S., Kato, T., Park, D., Sahai, E., Trepat, X., and Labernadie, A. (2021). CAFs and Cancer Cells Co-Migration in 3D Spheroid Invasion Assay. Methods Mol. Biol. *2179*, 243–256. https://doi.org/10.1007/978-1-0716-0779-4_19.

STAR★METHODS

KEY RESOURCES TABLE

REAGENT or RESOURCE	SOURCE	IDENTIFIER
Antibodies		
Anti-CD14 antibody	Abcam	Cat# ab183322; RRID: AB_2909463
Anti-CD45 antibody	Abcam	Cat# ab10558; RRID: AB_442810
Anti-AREG antibody	Proteintech	Cat# 66433-1; RRID: AB_2881803
Anti-EREG antibody	Biorbyt	Cat# orb378205
Mass cytometry antibody panel		See Table S2
Chemicals, peptides, and recombinant proteins		
Recombinant EREG	MedChemExpress	Cat# HY-P7011
Recombinant AREG	MedChemExpress	Cat# HY-P7002
Dulbecco's modified Eagle medium	Gibco	Cat# 11965092
Roswell Park Memorial Institute 1640 medium	Gibco	Cat# 11875119
Fetal bovine serum	Gibco	Cat# 11550356
Non-essential amino acids	Gibco	Cat# 11140050
Sodium pyruvate	Gibco	Cat# 11360070
Penicillin/streptomycin	Gibco	Cat# 15140122
DiO cell membrane dye	Beyotime Biotechnology	Cat# C1038
DiI cell membrane	Beyotime Biotechnology	Cat# C1036
Methylcellulose	Dieckmann	Cat# MD00291
Cultrex® RGF BME	R&D SYSTEMS	Cat# 3433-005-001
Collagen I	Gibco	Cat# A10483-01
Lipofectamine™ 3000	Invitrogen	Cat# L3000015
FOSL2 plasmid	Sino Biological	Cat# HG15308-ACG
Gefitinib	MedChemExpress	Cat# HY-50895
siRNA AREG 209	GenePharma	GCUCUUGAUACUCGGCUCATT UGAGCCGAGUAUCAAGAGCTT (5′-3′)
siRNA AREG 390	GenePharma	GGAUUUGAGGUUACCUCAATT UUGAGGUAACCUCAAAUCCTT (5′-3′)
siRNA AREG 348	GenePharma	UCUGGGAAGCGUGAACCAUTT AUGGUUCACGCUUCCCAGATT (5′-3′)
siRNA EGFR 456	GenePharma	GCAGAGGAAUUAUGAUCUUTT AAGAUCAUAAUUCCUCUGCTT (5′-3′)
siRNA EGFR 767	GenePharma	GCAACAUGUCGAUGGACUUTT AAGUCCAUCGACAUGUUGCTT (5′-3′)
siRNA EGFR 1068	GenePharma	GGAGAUAAGUGAUGGAGAUTT AUCUCCAUCACUUAUCUCCTT (5′-3′)
siRNA FOSL2 818	GenePharma	GGAUUAUCCCGGGAACUUUTT AAAGUUCCCGGGAUAAUCCTT (5′-3′)
siRNA FOSL2 1304	GenePharma	CCUGCAGAAGGAGAUUGCUTT AGCAAUCUCCUUCUGCAGGTT (5′-3′)
siRNA FOSL2 1643	GenePharma	GAACCUCGUCUUCACCUAUTT AUAGGUGAAGACGAGGUUCTT (5′-3′)
NucleoSpin RNA Plus kit	Takara	Cat# 740984.50
RIPA buffer	Thermo Fisher Scientific	Cat# 89901
Tris-HCl	Invitrogen	Cat# 15504-020
Dodecyl sulfate	TCI Development Co.	Cat# 151-21-3

(*Continued on next page*)

CellPress
OPEN ACCESS

Continued

REAGENT or RESOURCE	SOURCE	IDENTIFIER
Bromophonol blue	BIO-RAD	Cat# 161-0404
Glycerol	ChemCruz	Cat# SC-29096B
Deposited data		
Single-cell RNA-sequencing data	This study	GEO: GSE237779
TCGA data	Firehose	https://gdac.broadinstitute.org/
CGGA data	CGGA database	http://www.cgga.org.cn/
Cancer Cell Line Encyclopedia data	CCLE	https://sites.broadinstitute.org/ccle/
Ivy Glioblastoma Atlas Project data	IVY GAP	https://glioblastoma.alleninstitute.org/
Longitudinal glioblastoma patient data	SRA	SRP074425
Experimental models: Cell lines		
Human: glioblastoma cell line U251	Dr Hin Chu	https://doi.org/10.1016/S2666-5247(2030004-5)
Human: monocyte cell line THP-1	Dr Chi-Ping Chan	https://doi.org/10.1371/journal.ppat.1008611
Software and algorithms		
Seurat	(Stuart et al., 2019)[64]	https://satijalab.org/seurat/index.html
Cellranger	10X Genomics	https://support.10xgenomics.com/single-cell-gene-expression/software/pipelines/latest/using/count
Cytobank	Beckman Coulter	https://premium.cytobank.org/cytobank
SingleR	(Aran et al., 2019)[18]	https://rdrr.io/github/dviraran/SingleR/
InferCNV	(Patel et al., 2014)[65]	https://bioconductor.org/packages/release/bioc/html/infercnv.html
Slingshot	(Street et al., 2018)[66]	https://bioconductor.org/packages/release/bioc/html/slingshot.html
Monocle2 and Monocle3	(Cao et al., 2019; Qiu et al., 2017b, 2017a; Trapnell et al., 2014)[67–70]	http://cole-trapnell-lab.github.io/monocle-release/
Gene Set Enrichment Analysis	(Subramanian et al., 2005)[71]	https://www.gsea-msigdb.org/gsea/index.jsp
SCENIC	(Aibar et al., 2017)[45]	https://scenic.aertslab.org/
ConsensusClusteringPlus	(Wilkerson and Hayes, 2010)[72]	https://bioconductor.org/packages/release/bioc/html/ConsensusClusterPlus.html
Lifelines	(Davidson-Pilon, 2022)[73]	https://lifelines.readthedocs.io/en/latest/
SPATA2	(Ravi et al., 2022)[52]	https://github.com/theMILOlab/SPATA2

RESOURCE AVAILABILITY

Lead contact

Further information and requests for resources and reagents should be directed to and will be fulfilled by the lead contact, Jiguang Wang (jgwang@ust.hk).

Materials availability

This study did not generate new unique reagents.

Data and code availability

- Single-cell RNA-seq data have been deposited at GEO and are publicly available under accession numbers GEO: GSE237779. The data of TCGA GB patients are available in the Broad Institute Firehose platform (https://gdac.broadinstitute.org/). The data of CGGA GB patients are available in the CGGA website (https://cgga.org.cn/). The RNA-seq expression data of Ivy Glioblastoma Atlas Project are available on the data portal (https://glioblastoma.alleninstitute.org/static/download.html).
- This paper does not report original code.
- Any additional information required to reanalyze the data reported in this work paper is available from the lead contact upon request.

EXPERIMENTAL MODEL AND SUBJECT DETAILS

Patients and ethics statements

Peripheral blood samples and surgically resected tumor tissues were obtained from glioma patients undergoing craniotomy surgery at Beijing Tiantan Hospital (Beijing, China) from June 2018 to April 2019 after informed consent was provided. All cases were confirmed by histopathology. None of the patients used glucocorticoids before sampling. This research was approved by the Institutional Review Board (IRB) and Ethics Committee of Beijing Tiantan Hospital (Beijing, China). Each patient provided written informed consent.

Cell culture

Human glioblastoma cell line U251 was maintained in cell culture containing Dulbecco's modified Eagle medium (DMEM), supplemented with 10% fetal bovine serum (v/v) and 1% penicillin/streptomycin (v/v). Human monocytes THP-1 cells were cultured in Roswell Park Memorial Institute (RPMI) 1640 medium, supplemented with 10% fetal bovine serum (v/v), 1% penicillin/streptomycin (v/v), 1X non-essential amino acids and 1 mM of sodium pyruvate. All cells were kept in an incubator at 37°C and 5% CO2. All reagents were purchased from Gibco (Thermo Fisher Scientific, Massachusetts, USA).

METHOD DETAILS

GB specimens single-cell dissociation

After the operation ice-cold Dulbecco's phosphate-buffered saline (DPBS, D8537, Sigma-Aldrich, St. Louis, MO) was used to wash GB tissues immediately. Briefly, the GB specimens were dissociated using type IV collagenase (17104019, GIBCO, Gaithersburg, MD) (10 min at 37°C). The specimens were then washed with Dulbecco's Modified Eagle's Medium (DMEM, D5796, Sigma-Aldrich, St. Louis, MO) and centrifuged (4 min at 300 g with minimal braking). A 70 μm cell strainer were used to filter the specimens in DPBS. The filtered cell suspension was washed with red blood cell (RBC) lysis buffer (555899, BD Biosciences, Franklin Lakes, NJ) and with DPBS. The resulting cell pellet was then resuspended in 1 mL staining buffer (DPBS containing 5% fetal bovine serum, FBS; 0500, ScienCell, Carlsbad, CA) and washed one more time. Single-cell specimens were prepared for CyTOF examination or single-cell RNA Sequencing.

Peripheral blood single-cell dissociation

Peripheral blood was collected into ethylenediaminetetraacetic acid anticoagulation coated tubes. The specimens were first centrifuged (5 min at 800 g with minimal braking) to remove plasma. Then, the specimens were transferred into SepMate PBMC isolation tubes containing Ficoll (86450, STEMCELL Technologies, Vancouver, Canada) and centrifuged (10 min at 1200 g with minimal braking). Pelleted cells were then washed with RBC lysis buffer. The blood cell pellet was resuspended in 1 mL staining buffer followed by washing to remove excessive stain. Single-cell specimens were prepared for CyTOF examination or single-cell RNA Sequencing.

Mass cytometry

A panel of 27 antibodies was designed to distinguish immune cells from GB patients. Antibodies were either purchased in a preconjugated form from Fluidigm (South San Francisco, CA) or in a purified form from Biolegend (San Diego, CA). Purified antibodies were conjugated in-house using the Maxpar X8 Multimetal Labeling Kit (201300, Fluidigm, South San Francisco, CA) according to the manufacturer's recommendations. The antibodies and reporter isotopes are summarized in Table S2. For cell preparation, cell specimens were rapidly rewarmed. Cell specimens were first stained with cell surface antibodies for 30 min on ice. Subsequently, the specimens were permeabilized (4°C overnight) and stained with intracellular antibodies for 30 min on ice. The antibody-labeled specimens were washed and incubated in 0.125 nM intercalator-Ir (201192B, Fluidigm, South San Francisco, CA) diluted in phosphate-buffered saline (PBS, 806544, Sigma-Aldrich, St. Louis, MO) containing 2% formaldehyde and stored at 4°C until mass cytometry examination. Before acquisition, the specimens were washed with deionized water and then resuspended at a concentration of $1*10^6$ cells/mL in deionized water containing a 1:20 dilution of EQ Four Element Beads (201078, Fluidigm, South San Francisco, CA). The specimens were then examined by CyTOF2 mass cytometry (Fluidigm, South San Francisco, CA).

Single-cell RNA sequencing

The GB or peripheral blood cell suspension was loaded into Chromium microfluidic chips with 3' (v3) chemistry and barcoded with a 10× Chromium Controller (10X Genomics). RNA from the barcoded cells was subsequently reverse-transcribed and sequencing libraries constructed with reagents from a Chromium Single Cell 3' (v3) reagent kit (10X Genomics) according to the manufacturer's recommendations. Sequencing was performed with Illumina (NovaSeq) according to the manufacturer's recommendations (Illumina).

CyTOF data analysis

CyTOF data were obtained in fcs formed files. The addition of EQ Four Element Beads allowed us to use the MATLAB-based normalization technique using bead intensities as previously described.[74] The CyTOF data were uploaded and analyzed on Cytobank.[75] Cell

CellPress
OPEN ACCESS

type recognition parameters for CyTOF were summarized in Table S3. Manual gating was applied to mark cell types as previously reported.[76] Data were analyzed using viSNE algorithms on the indicated gated cells.[77]

Analysis of single-cell RNA sequencing data

Raw data of each sample was preprocessed using Cell Ranger,[78] and the filtered expression matrix was obtained and analyzed with Seurat.[64] The high-quality cells were further selected by: (1) 600–3000 genes were detected; (2) at least 3000 UMIs were counted; (3) the fraction of mitochondrial genes was below 20%. The selected cells in each sample were further characterized by clustering and cell type annotation. After selecting the top 2000 variable genes for principal component analysis (PCA), the principal components (PCs) above the elbow point were selected as features for clustering and dimensionality reduction by t-SNE. Clustering was performed using Louvain's method at resolution of 1. The annotation of major cell types in was conducted by matching each cluster with criteria of marker combinations used in CyTOF (Table S3), and the annotation of cell subtypes was conducted by a combined approach of manual inspection of classical markers[17,19] and automatic cell type detection by SingleR,[18] which compares each single cell and cluster to purified cell types in reference datasets. Single cells from different samples were merged by the canonical component analysis (CCA) method in Seurat. The removal of batch effect was examined by observing well-mixed sample labels in the t-SNE plot, while the cell type labeled in the analysis of individual samples are well aligned with the clusters on the merged data. The dimensionality reduction, re-clustering and identification of cell subtypes, and trajectory analysis was conducted on the merged data. The classification of transcriptome subtypes and prediction of copy number alterations of tumor cells in single-cell RNA-sequencing data was performed following the methods in previous studies.[44,65]

Single-cell trajectory analysis

The trajectory of monocyte-MDM transformations was performed by Slingshot,[66] Monocle2 and Monocle3.[67–70] Prior to constructing the trajectory, the expression data of cells from different samples were merged with CCA in Seurat. The top 2000 variable genes were selected for PCA analysis, and the PCs with standard variation above the elbow point were selected for dimensionality reduction with t-SNE, UMAP, ICA or DDRTree.

Identifying Mono/Macro subtypes

The microglia- and MDM-specific gene sets were obtained from the study by Müller et al.[11] Principal component analysis and consensus clustering[72] of all monocytes and macrophages in PBMC, epilepsy, astrocytoma and GB samples were performed based on the expression of microglia- and MDM-specific genes. In the consensus clustering method, the cell-cell similarity was measured by Euclidian's distance and clustered by hierarchical clustering combined with Ward's method, and 1000 permutations were performed for k ranging from 2 to 10 classes. In each permutation, 80% of samples were selected and clustered. The method ensures cluster stability and robustly. Cophenetic correlation coefficient (ρ_k) was computed for each k to select the one with the largest ρ_k, as the Pearson correlation of the Euclidean distance induced by the consensus matrix C and the dendrogrammatic distance induced by the complete linkage used in the reordering of C.[79]

Differential expression and pathway activity analysis

The significantly differentially expressed genes (DEGs) between two groups of cells analyzed are defined by: (1) Benjamini-Hochberg adjusted p-value for Wilcox's rank-sum test <0.05; (2) differences in the percentage of cells that express the gene in the two groups were larger than 0.2. Differential gene expression analysis between two groups of patients were calculated by Wilcox's rank-sum test. Comparison of pathway activity between two groups of patients or cells was performed by Gene Set Enrichment Analysis (GSEA).[71]

Scoring MG, MDM, monocyte and TAMo abundance in bulk RNA sequencing data

The MG-, MDM- and monocyte-specific markers were defined as a subset of ontogeny-specific markers[11] that can distinguish the three cell subtypes and were invariant regardless of tissue of origin. The selected markers were shown in Figure 2C and applied in estimating the cell type abundance in bulk RNA sequencing data of TCGA glioma patients by calculating the average expression of the gene sets in each sample. In the analysis of TAMo-specific markers, genes with significantly elevated expression in TAMo and low expression in other monocyte and MDM subgroups (expressed in less than 20% of non-TAMo populations) were selected.

Survival analysis

Survival analysis was performed with python package 'lifelines'. The associations between the cell type score and overall survival was estimated according to previous methods,[80] which segregated patients into high-expression and low-expression groups by different cut-offs of FPKM level and calculating the p-value by log rank test, and the most significant p-value was reported.

Scoring mesenchymal transformation in paired samples from the same patient

To capture the changes in mesenchymal gene signature in longitudinally paired samples collected from the same patient while avoiding batch effects, we converted the log2-transformed FPKM into ranks of each gene amongst all protein coding genes in the sample. The rank-change of each gene between the recurrent and initial sample was calculated, and further applied in single-sample GSEA

analysis.[79] The four gene sets corresponding to the four GB transcriptome subtypes was assessed, and patients with significant elevated mesenchymal subtype signatures (with normalized enrichment score for mesenchymal signature $S_{MES} > 2$ and $p < 0.01$) were defined as positive cases for mesenchymal transformation. In the longitudinal patient cohort, we analyzed the mesenchymal transformation during recurrence in 57 GB patients that: (1) contained bulk RNA-seq data of both initial and recurrent tumor; (2) were not hypermutated during recurrence. The TAMo infiltration score S_{TAMo} was calculated as the TAMo score of the recurrence tumor eliminated by that of the initial tumor.

Single-cell transcriptional network analysis

The gene expression matrix of monocytes and MDMs were applied as the input for transcriptional network analysis using default parameters in SCENIC.[45] In the first step, the GRNBoost method was applied to identify coexpression of TF and potential targets. In the second step, the regulon of each TF was refined either by searching for TF binding motifs in the 500bp-upstream sequence of transcription start sites of the coexpressed targets (hereafter termed "motif analysis") or by overlapping with TF-bound peaks in ChIP-seq data (hereafter termed "ChIP-seq analysis"). As the number of TFs available in the ChIP-seq database was limited, we applied the regulons inferred from motif analysis in the third step of SCENIC, which aggregated these regulons into AUC scores of TFs. Based on the AUC matrix, we conducted hierarchical clustering as the examples in the SCENIC paper and unbiasedly identified a cluster of TAMo-specific TFs. The list of TAMo-specific TFs was further prioritized by whether the TF was over-expressed in TAMo and whether EREG and AREG were regulated by the TF.

Glioblastoma proteomic data analysis

The public data used in this validation were generated by the Clinical Proteomic Tumor Analysis Consortium (NCI/NIH) and downloaded from the supplementary materials.[35] The 110 samples were filtered based on the sample types (tumor only), the molecular subtypes (IDH-wildtype only), and only the samples with both EGFR mutation status and EGFR copy number variation (CNV) status are kept. Finally, 89 IDH-wildtype GB samples were included in the analysis. The EGFR-altered samples were defined as samples having either EGFR mutation or amplification. In total, 12 samples were classified as EGFR-wildtype samples. As not all of the TAMo signature genes were provided in the proteomic data, the TAMo scores of each sample were calculated using RNA sequencing data. The raw FPKM-UQ values of RNA sequencing were obtained, processed by log-transformation and gene-wise *Z* score scaling. Then, the TAMo score was generated as the mean *Z* score values of the TAMo-specific genes (*EREG, AREG, CXCL2, MARCO, LRG1,* and *VEGFA*) for each sample. The Spearman's correlation test was used to determine the relation between TAMo score and various phosphorylation sites' abundance (EGFR-Y1172, EGFR-Y1197, STAT3-S727) among the EGFR-wildtype IDH-wildtype GB samples.

Glioblastoma spatial transcriptome data analysis

The spatial transcriptomic dataset[52] was downloaded and analyzed. Histological regions were defined in the original study. The TAMo score and mesenchymal score for different histological regions were calculated based on normalized expression. Scaled expression levels of marker genes and signature scores amongst different histological regions of each sample were visualized by SPATA2, an R tool developed for spatial transcriptomic data analysis.

siRNA transfection and reverse transcription-PCR

All siRNAs were from GenePharma (SH, China) and FOSL2 plasmid was from sinobiological (SH, China). Lipofectamine 3000 purchased from Invitrogen (CA, USA) was used for siRNA transfection. Target gene expression was then quantified by reverse transcription-polymerase chain reaction (RT-PCR), Briefly, total RNA was extracted using total RNA extraction reagent (Takara Bio, USA) according to manufacturer's instructions. Total RNA was reverse transcribed into single-stranded cDNA by thermal cycler (Applied Biosystems, Thermo Fischer Scientific) prior to gene quantification by LightCycler 480 System (Roche Diagnostics) following standard procedures.

Trans-well invasion assay

Cells migration and invasion assay were conducted on the Corning Trans-well 3422 24-well plates (8 μm pore size). Collagen I diluted with 6 mM acetic acid was added on the upside of polycarbonate membrane at 4°C and gelled for 1 h at 37°C U251 cells were seeded on the upper chamber in serum-free medium. In the non-contacting co-culture model, THP-1 cells were placed in the lower chamber. After incubation for 18 h, the cells invaded through the polycarbonate membrane were fixed with 4% paraformaldehyde and stained with 0.1% crystal violet staining solution. Images were then captured by a standard microscope (Nikon Eclipse Ts2).

3D spheroid invasion assay

3D cell spheroids were generated from cultured cells by using hanging-drop method.[81,82] Prior to spheroids formation, cells were fluorescently labeled with DiO or DiI cell membrane dyes (C1038/C1036, Beyotime Biotechnology, China). Cells were detached and suspended with 0.24% methylcellulose (MD00291, Dieckmann, China) in medium. Droplets (15 μL) containing 8000 cells were placed onto the inner surface of a culture dish lid which was subsequently turned upside-down resulting in hanging droplets. Co-culture spheroids were prepared by mixing THP-1 and U251 cell suspension (1:1, v/v) prior to droplets formations. After 16 h, spheroids were harvested and embedded in a 8-well chamber slide with extracellular matrix containing 6 mg/mL matrigel (Cultrex

CellPress
OPEN ACCESS

RGF BME, 3433-005-001, Bio-Techne, Minneapolis, USA) and 1.4 mg/mL collagen (Gibco Collagen I, A10483-01, Massachusetts, USA). Medium with 200 ng/mL of amphiregulin (AREG, HY-P7002, MedChemExpress, China) and 200 ng/mL epiregulin (EREG, HY-P7011, MedChemExpress, China) were added on top of the solidified matrix, and spheroid cultures were maintained at 37°C and 5% CO_2 to enable spheroid growth and invasion into the 3D matrix. Blank medium was added to the control group. Images of 3D spheroids were captured by a Zeiss LSM 900 confocal microscope with 15 μm thick z-stacks. 2D images were then generated using maximum projection in Zeiss Zen Blue software for analysis. Quantifications of cell invasion were determined by the ratio of the protrusion area over the core area of each spheroid.

Immunofluorescence staining

GB specimens were fixed in 4% PFA/PBS overnight at 4°C, dehydrated in 100% ethanol, and embedded in paraffin. Tissue sections with thickness of 3 μm underwent dewaxing and rehydration through xylene and ethanol treatment were subsequently used for staining. Then, the Opal Multiplex IHC Assay Kit (PerkinElmer, USA) was used for the paraffin-embedded tissue sections according to the manufacturer's instructions. Images were acquired on LSM 710 (Zeiss, Germany). Primary antibodies were: anti-CD14 (1:100, ab183322, abcam), anti-CD45 (1:200, ab10558, abcam), anti-EREG (1:200, orb378205, biorbyt), anti-AREG (1:200, 66433-1, proteintech).

QUANTIFICATION AND STATISTICAL ANALYSIS

No statistical methods were used to predetermine sample size. For cell-based culture experiments, biological triplicates were performed in each single experiment in general, unless otherwise states. Statistical analysis were performed using R 4.2.0 and Python 3.6 software. Two-tailed paired t-test and Wilcox's rank-sum test were used and stated in the figures and legends. Details of CyTOF and scRNA-seq data analysis are stated in the method details.